Brain Structure and Function (2019) 224:1469–1488
https://doi.org/10.1007/s00429-019-01844-6

ORIGINAL ARTICLE

Along-axon diameter variation and axonal orientation dispersion revealed with 3D electron microscopy: implications for quantifying brain white matter microstructure with histology and diffusion MRI

Hong-Hsi Lee[1,2] · Katarina Yaros[1] · Jelle Veraart[1] · Jasmine L. Pathan[1] · Feng-Xia Liang[3] · Sungheon G. Kim[1,2] · Dmitry S. Novikov[1,2] · Els Fieremans[1,2]

Received: 23 April 2018 / Accepted: 1 February 2019 / Published online: 21 February 2019

Abstract

Tissue microstructure modeling of diffusion MRI signal is an active research area striving to bridge the gap between macroscopic MRI resolution and cellular-level tissue architecture. Such modeling in neuronal tissue relies on a number of assumptions about the microstructural features of axonal fiber bundles, such as the axonal shape (e.g., perfect cylinders) and the fiber orientation dispersion. However, these assumptions have not yet been validated by sufficiently high-resolution 3-dimensional histology. Here, we reconstructed sequential scanning electron microscopy images in mouse brain corpus callosum, and introduced a random-walker (RaW)-based algorithm to rapidly segment individual intra-axonal spaces and myelin sheaths of myelinated axons. Confirmed by a segmentation based on human annotations initiated with conventional machine-learning-based carving, our semi-automatic algorithm is reliable and less time-consuming. Based on the segmentation, we calculated MRI-relevant estimates of size-related parameters (inner axonal diameter, its distribution, along-axon variation, and myelin *g*-ratio), and orientation-related parameters (fiber orientation distribution and its rotational invariants; dispersion angle). The reported dispersion angle is consistent with previous 2-dimensional histology studies and diffusion MRI measurements, while the reported diameter exceeds those in other mouse brain studies. Furthermore, we calculated how these quantities would evolve in actual diffusion MRI experiments as a function of diffusion time, thereby providing a coarse-graining window on the microstructure, and showed that the orientation-related metrics have negligible diffusion time-dependence over clinical and pre-clinical diffusion time ranges. However, the MRI-measured inner axonal diameters, dominated by the widest cross sections, effectively decrease with diffusion time by ~17% due to the coarse-graining over axonal caliber variations. Furthermore, our 3*d* measurement showed that there is significant variation of the diameter along the axon. Hence, fiber orientation dispersion estimated from MRI should be relatively stable, while the "apparent" inner axonal diameters are sensitive to experimental settings, and cannot be modeled by perfectly cylindrical axons.

Keywords 3*d* electron microscopy · Axonal diameter variation · 3*d* axon segmentation · Corpus callosum · Fiber orientation distribution · Axonal diameter distribution · *g*-Ratio · Diffusion coarse-graining · Diffusion time-dependence

Introduction

Diffusion MRI (dMRI) is a non-invasive imaging modality that, by measuring the random motion of water molecules at NMR-accessible diffusion times ($t \sim 1$–1000 ms), is sensitive to length scales $L(t) \sim 1$–50 μm, comparable to cell sizes (Jones 2010; Novikov et al. 2018a). Several tissue models for dMRI have been proposed to specifically probe the neuronal microstructure, to estimate the axon orientation dispersion (Jespersen et al. 2007, 2010, 2017; Novikov et al. 2018c; Reisert et al. 2017; Ronen et al. 2014; Schilling et al. 2018; Sotiropoulos et al. 2012; Tariq et al. 2016; Zhang et al. 2012)

✉ Hong-Hsi Lee
Honghsi.Lee@nyulangone.org

[1] Department of Radiology, Center for Biomedical Imaging, New York University School of Medicine, 660 First Avenue, New York, NY 10016, USA

[2] Center for Advanced Imaging Innovation and Research (CAI2R), New York University School of Medicine, 660 First Avenue, New York, NY 10016, USA

[3] Department of Cell Biology and Microscopy Core, New York University School of Medicine, 540 First Avenue, New York, NY 10016, USA

and the axonal diameter distribution (Alexander et al. 2010; Assaf et al. 2008; Barazany et al. 2009; Benjamini et al. 2016; Duval et al. 2015; Komlosh et al. 2013). To enable parsimonious dMRI modeling, assumptions have been made, which so far have not been fully validated by comparing against histology. In particular, axons are assumed to be circular cylinders for simplicity, and diameter variations along each axon are typically neglected (Alexander et al. 2010; Assaf and Basser 2005; Assaf et al. 2008).

The above perfect-cylinder assumption still needs to be confirmed with histology. So far, changes in axonal caliber or diameter have been reported as varicosities or boutons in unmyelinated axons of rat hippocampus and cerebellum (Shepherd et al. 2002) and of rat cortical neurons in vitro (Tang-Schomer et al. 2012), or as neurite beadings of rat sciatic nerves induced in vitro by stretching (Budde and Frank 2010). Recently, axonal diameter variations along myelinated axons have been observed in both normal and injured rat optic nerves (Giacci et al. 2018). Here, we acquired 3*d* high-resolution electron microscopy (EM) images of mouse corpus callosum, segmented myelinated axons, and estimated histology-based tissue parameters, such as axonal size and its distribution and variation along the axon, as well as orientation dispersion.

So far, previous studies focused on validating dMRI models in brain WM against histology, and reported multiple microstructure parameters, including the fiber orientation distribution (FOD) (Grussu et al. 2016; Mollink et al. 2017; Ronen et al. 2014; Schilling et al. 2016, 2018), axon dispersion angle (Ronen et al. 2014), inner axonal diameter (Abdollahzadeh et al. 2017; Aboitiz et al. 1992; Caminiti et al. 2009; Kleinnijenhuis et al. 2017; Liewald et al. 2014; Mason et al. 2001; West et al. 2015), and *g*-ratio (Abdollahzadeh et al. 2017; Kleinnijenhuis et al. 2017; Mason et al. 2001; Stikov et al. 2015; West et al. 2015, 2016; Yang et al. 2016). In histology, size-related quantities, e.g., diameter and *g*-ratio, were estimated either by 2*d* (Aboitiz et al. 1992; Caminiti et al. 2009; Liewald et al. 2014; Mason et al. 2001; West et al. 2015) or 3*d* high-resolution EM images (Abdollahzadeh et al. 2017; Kleinnijenhuis et al. 2017). In contrast, the orientation-related metrics, e.g., FOD and dispersion angle, were evaluated either by 2*d* low-resolution polarized light images (4 μm/pixel, in-plane) (Mollink et al. 2017), light microscopy images (1–1.6 μm/pixel, in-plane) (Grussu et al. 2016; Ronen et al. 2014), or by 3*d* moderate-resolution confocal microscopy images (0.42 μm/slice, through plane) (Schilling et al. 2016, 2018). Although the tissue anisotropy index has been evaluated on 3*d* EM images (Salo et al. 2018), retrieving other orientation metrics, e.g., FOD, its rotational invariants and the dispersion angle, from 3*d* high-resolution EM images ($\lesssim$0.1 μm/slice, through plane) has not yet been attempted.

Furthermore, definitions of tissue parameters differ between studies, both in histology and MRI, and need to be clarified before use. In particular, the orientation dispersion of axon bundles could be summarized by (1) the standard deviation (SD) of dispersion angles projected on a 2*d* plane (Ronen et al. 2014), by (2) rotational invariants and the root-mean-square (rms) of the dispersion angle's cosine for spherical harmonics (SH)-based methods (Jespersen et al. 2017; Novikov et al. 2018c; Reisert et al. 2017), or by (3) the normalized orientation dispersion index (ODI) of specific orientation distributions (e.g., Watson or Bingham distributions) (Schilling et al. 2018; Tariq et al. 2016; Zhang et al. 2012). In this study, we focus on the first two definitions to avoid introducing further assumptions on the functional form of the axon dispersion.

Similarly, axonal diameters have been estimated using various methods, discussed in details further in "Appendix B". To avoid overestimation of the inner axonal diameter caused by obliquely sliced axons, most of the 2*d* histological studies measured the inscribed circle diameter as the diameter estimate (Aboitiz et al. 1992; Caminiti et al. 2009; Liewald et al. 2014). Other histological studies adopted an equivalent circle diameter calculated by the cross-sectional area (West et al. 2015) or the short axis length of a fitted ellipse (Abdollahzadeh et al. 2017). In this study, we focus on the equivalent circle diameter, since (1) the 3*d* axon structure is fully reconstructed and free from problems of oblique cross sections and (2) contours of the intra-axonal space and the myelin sheath might be different, leading to unreliable estimates of the *g*-ratio (ratio of inner to outer diameter) when using other definitions.

Aside from ambiguous definitions of microstructural features, comparison between dMRI and histology depends on the experimental settings of the dMRI experiment. Indeed, the diffusion process can be approximately understood as a coarse-graining process, which is equivalent to smoothing the tissue microstructure (Novikov et al. 2014, 2018a) using a kernel of a width commensurate with the diffusion length $L \propto \sqrt{t}$. In other words, the diffusion times applied in dMRI measurements potentially affect the quantitative estimates between studies using different acquisition parameters; accounting for such biases will be important for the future precision tests of microstructural models.

Here, by analyzing segmented myelinated axons, we calculated both orientation-related and size-related axonal features based on definitions from either histology or MRI experiment, where the effect of varying diffusion time was simulated by applying a corresponding smoothing kernel, and demonstrated a non-trivial discrepancy between estimated microstructural characteristics from both definitions. In particular, we demonstrated by 3*d* high-resolution EM segmentation, for the first time, the influence of the diffusion

time-dependence on the orientation dispersion and the inner axon diameter.

To achieve our goals of quantifying sizes and orientations of WM axons, we had to develop a 3*d* segmentation algorithm. So far, many EM segmentation software tools have been released for segmenting gray matter images that use semi-automatic analysis with an interactive proofreading interface (Dorkenwald et al. 2017; Kaynig et al. 2015; Sommer et al. 2011). Such methods require abundant training data, for which generation is very labor-intensive and time-consuming. In WM, however, appropriate EM segmentation methods are still limited (Abdollahzadeh et al. 2017; Kleinnijenhuis et al. 2017; Zaimi et al. 2018). To segment myelinated axons within acceptable processing time, we propose and validate here a semi-automatic segmentation algorithm depending on diffusion trajectories obtained by random-hopping on a cubic lattice bounded by a binary myelin mask, as a simplified version of the seeded-region-growing method (Abdollahzadeh et al. 2017; Adams and Bischof 1994).

Materials and methods

All procedures performed in studies involving animals were in accordance with the ethical standards of New York University School of Medicine. All mice were treated in strict accordance with guidelines outlined in the National Institutes of Health Guide for the Care and Use of Laboratory Animals, and the experimental procedures were performed in accordance with the Institutional Animal Care and Use Committee at the New York University School of Medicine. This article does not contain any studies with human participants performed by any of the authors.

Animals and image acquisition

A female 8-week-old C57BL/6 mouse was perfused transcardiacally using a fixative solution of 4% PFA, 2.5% glutaraldehyde, and 0.1 M sucrose in 0.1 M phosphate buffer (PB, pH 7.4). The genu of corpus callosum (CC) was later excised from the midsagittal slice of the dissected brain, and the tissue was sampled from the central region of the genu and was fixed in the same fixative solution, followed by a PB containing 2% OsO4 and 1.5% potassium ferrocyanide for 1 h. The tissue was then stained with 1% thiocarbohydrazide (Electron Microscopy Sciences, EMS, PA) for 20 min, 2% osmium tetroxide for 30 min, and 1% aqueous uranyl acetate at 4 °C overnight. An En Bloc lead staining was performed at 60 °C for 30 min to enhance membrane contrast. The brain sample was dehydrated in alcohol and acetone, and embedded in Durcupan ACM resin [EMS, PA (Wilke et al. 2013)]. The tissue sample was analyzed with a scanning electron microscope (SEM) (Zeiss Gemini 300 SEM with 3View) at high-vacuum pressure, and 401 consecutive images of 6000×8000 pixels were acquired, representing a volume of $36 \times 48 \times 40.1\ \mu m^3$ with a voxel size of $6 \times 6 \times 100\ nm^3$.

Image processing and axon segmentation by random-walker algorithm (RaW)

We down-sampled the image to a resolution of $24 \times 24 \times 100\ nm^3$ using Lanczos interpolation to lower the computational cost without compromising the segmentation accuracy. Furthermore, we corrected the geometric distortion in slices disagreeing with the interpolation estimated from adjacent slices (two slices above and two slices below): The first 200 images (slice 1–200) showed no distortion, with an exception of one image with mild distortion corrected using a non-linear deformation calculated with optical flow estimation (Sun et al. 2010, 2014). As the following 201 slices (slice 201–401) contained significantly more unusable slices with either intractable distortions, signal dropouts or complete signal loss, we excluded these from further analysis. Hence, we selected a subset of 200 slices ($36 \times 48 \times 20\ \mu m^3$ in volume) to rule out slices with intractable distortions (Fig. 1a).

To semi-automatically segment the intra-axonal space (IAS) of myelinated axons, we employed a random-hopping diffusion process, dubbed random-walker algorithm (RaW), as a simplified seeded-region-growing algorithm (Adams and Bischof 1994) applied on a binary mask: we manually seeded an initial position per axon within the central slice (451 seeds in Fig. 1c), and filled the IAS by diffusion trajectories, obtained by random-hopping on a cubic lattice, of 4000 particles per axon with 640,000 steps. The diffusion trajectory is confined by a myelin mask (Fig. 1b) obtained using a pixelwise classifier (Sommer et al. 2011). Segmented axons with an imperfect myelin mask were deleted by proofreading, resulting in an IAS mask of 321 segmented axons (59,231 axon cross sections). The IAS segmentation was then completed by automatically seeding within the previously generated diffusion trajectories confined by the non-leaky myelin mask (Fig. 1d). The seeding density is a seed per ten slices for each axon, filled with 10,000 particles per seed with 40,000 steps. The IAS mask was down-sampled into $(100\ nm)^3$-resolution to further analyze axon geometries, e.g., fiber dispersion, axonal diameter, myelin thickness, and *g*-ratio.

All the processing was implemented in Matlab and accelerated by parallel computation with 12 CPU cores. Total processing time, including the manual seeding, numerical computations and the proofreading, was 2 days.

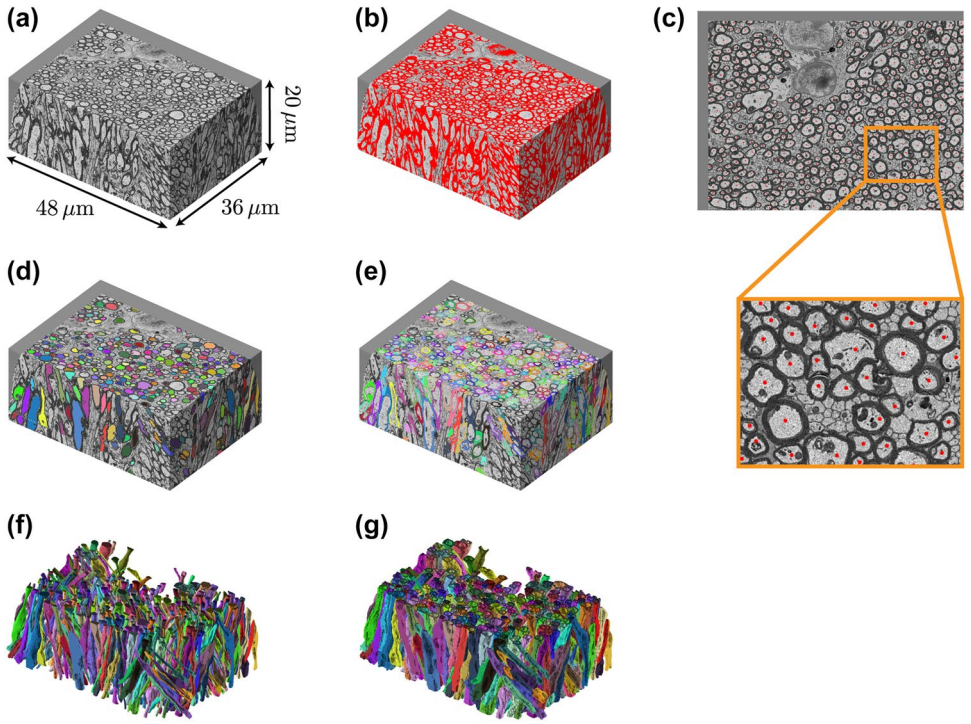

Fig. 1 Semi-automatic IAS segmentation pipeline. **a** Tissue sample of genu in CC, in a volume of $36\times48\times20$ μm^3, was acquired by sequential SEM. **b** Myelin mask (red) was obtained using a pixelwise classifier for further segmentation of the intra-axonal space (IAS). **c** Seeds (red dots) for random diffusion grid-hopping process were assigned manually over one central slice (451 seeds). The random-hopping trajectory was bounded by the myelin mask in **b**. **d** IAS (colors) was filled by all random-hopping trajectories (321 segmented IAS). The IAS from axons with leaky myelin mask has been excluded by proofreading. **e** Individual myelin sheath (colors) is the overlap of the myelin mask and the expanded IAS dilated by $\leq$0.4 μm. Touching myelin sheaths of adjacent axons are separated based on a non-weighted watershed algorithm. **f**, **g** By transforming each segmented IAS and individual myelin sheath into polyhedrons, it is feasible to perform numerical simulations in such 3*d* realistic microstructure

Ground-truth axon segmentation

To compare RaW to ground-truth, the IAS of 97 selected axons was manually carved by K.Y. and J.P., using the Carving function (Straehle et al. 2011) in ilastik software package (Sommer et al. 2011) as an initialization tool to speed up the brute-force manual segmentation process. Interactive seeded watershed segmentation was performed by ilastik with following settings:

1. Each 2*d* image (resolution = 24×24 nm^2) was smoothed by a kernel with a size of 1.6 pixel (38.4 nm), and was filtered to enhance edges, e.g., cell membrane, mitochondria and myelin sheath.
2. Markers inside the IAS (object markers) and outside the IAS (background markers) were manually assigned in multiple slices to initiate the Carving process in ilastik and connect the IAS across the image layers. Markers were further added to refine or correct the initial segmentation while proofreading. This manual correction step was necessary, especially for mitochondria attached to the myelin sheath, and nodes of Ranvier.

The segmentation was further verified by H.-H.L. and F.L. The total processing time was about 12 weeks.

The comparison of segmentations from both methods is based on the Jaccard index and the Sørensen–Dice index computed for individual IAS segmentations, and the foreground-restricted Rand F-score (V^{rand}) and the information theoretic F-score (V^{info}) (Arganda-Carreras et al. 2015) computed for IAS segmentations of all axons. The Jaccard index for each axon is the pixel number of the intersection divided by the pixel number of the union of IAS segmentations from both methods. The Sørensen–Dice index for each axon is the pixel number of the intersection divided by the average pixel number of IAS segmentations from both methods. The foreground-restricted rand F-score and the information theoretic F-score are closely related to the Rand index and the variation of information, respectively (Arganda-Carreras et al. 2015).

Inner axonal diameter

To quantify the effective axonal diameters or calibers from 3*d* histology, we aligned each axon's main direction (denoted

as $\hat{z}_{\text{axon}}$) parallel to the z-axis, cutoff 1 μm at both ends, to create the axon skeleton (a line connecting the center of mass of each slice), and calculated the cross-sectional area Ω for each slice perpendicular to the skeleton. Assuming an axon as a circular cylinder, its inner diameter is defined as the diameter of an equivalent circle with the same area: $2r \equiv 2\sqrt{\Omega/\pi}$. The along-axon variation of inner diameter is then estimated by the coefficient of variation of equivalent circle inner diameter $2r(\hat{z}_{\text{axon}})$, i.e., $\text{CV}(2r) \equiv \frac{\text{SD}(2r)}{\text{mean}(2r)}$, along each axon's main direction $\hat{z}_{\text{axon}}$.

In addition, we also compared the various definitions for the inner axonal diameter, such as the short and long axis length of the fitted ellipse with its second moments given by those of the axon cross section, and the inscribed circle diameter calculated by employing the distance transform to the axon cross section.

To simulate the microstructure coarse-grained by diffusion (Novikov et al. 2018a, b), the variation of the cross-sectional area along each segmented axon was smoothed by a Gaussian kernel with a variance $\sigma^2 = L^2/4$ (Novikov et al. 2014), where L is the diffusion length $\sqrt{2Dt}$, $D = 2$ μm^2/ms is a typical value for the intrinsic intra-axonal diffusion coefficient (Dhital et al. 2019; Novikov et al. 2018c; Veraart et al. 2018a, b), and $t = [1, 10, 100]$ ms are the characteristic diffusion times covering pre-clinical (~1–10 ms) and clinical (~10–100 ms) dMRI. The coarse-grained equivalent circle diameter was calculated accordingly.

Myelin sheath and *g*-ratio

Myelin sheaths of adjacent axons often touch each other, and are difficult to specify for each axon solely using the myelin mask. To segment each axon's individual myelin sheath (Fig. 1e), we overlapped the myelin mask and the expanded IAS segmentation (Kleinnijenhuis et al. 2017), which is dilated by a myelin thickness upper bound = 0.4 μm, a biologically plausible value for myelinated axons in the brain WM (see also "Limitations", "Discussion" and "Appendix A" for further explanations). Cases of adjacent axons with touching myelin sheath are further segmented by applying a non-weighted distance transform and watershed on the binary mask including all of the segmented IAS.

Next, the outer diameter was estimated as $2r' \equiv 2\sqrt{\Omega'/\pi}$, where the cross-sectional area Ω', perpendicular to the axon skeleton, contains both the IAS and the myelin sheath. The along-axon variation of outer diameter is estimated by the coefficient of variation of $2r'$, i.e., $\text{CV}(2r') \equiv \frac{\text{SD}(2r')}{\text{mean}(2r')}$, along each axon's main direction. The g-ratio was defined as $g \equiv r/r' = \sqrt{\Omega/\Omega'} \leq 1$.

The above g-ratio estimations were calculated based on a myelin sheath segmentation using a myelin thickness upper bound = 0.4 μm. To further evaluate the influence of the myelin thickness upper bound on estimated g-ratio values, we varied the upper bound from 0.1 to 0.6 μm and calculated the g-ratio accordingly.

Fiber orientation distribution

For the segmented IAS of each axon, the axon skeleton connecting all centers of mass in each slice was computed. To mimic the microstructure coarse-grained by diffusion, the piecewise linear skeleton of each segmented axon was then smoothed by a Gaussian kernel with a variance $\sigma^2 = L^2/4$ used as in section "Inner axonal diameter", "Materials and methods". For each degree of coarse-graining due to finite t, the tangent vector of the fiber skeleton was projected on a $3d$ triangulated spherical surface (Womersley 2017) to form the FOD, which was further decomposed with a spherical harmonics basis up to the order $l = 10$ to reconstruct the $3d$ glyph representation (Politis 2016).

Dispersion angle

The dispersion angle of axon segments was calculated using definitions both in $2d$ and $3d$, to compare to the corresponding $2d$ histological observations and $3d$ dMRI measurements, respectively.

In conventional histology, e.g., $2d$ light or electron microscopy, each image is a $2d$ cross section of a $3d$ structure. To compare our results with previous $2d$ histological studies, we projected all the axon segments onto a projection plane parallel to the bundle's mean direction at an azimuthal angle ϕ, and calculated the projected dispersion angle $\theta_{2d}(\phi)$, defined by the standard deviation of angles between the projected segments and the mean bundle direction, along which we rotated the projection plane (see "Appendix C" for details).

The true dispersion angle should of course be defined in $3d$. Given that the uniform measure on a sphere is given by $d(\cos\theta)$, it is natural to employ the rms of $\cos\theta$ and define an effective dispersion angle:

$$\theta_{\text{eff}} \equiv \cos^{-1}\sqrt{\langle\cos^2\theta_i\rangle}, \tag{1}$$

where the individual axon segment's dispersion angle θ_i is the angle between the axon segment's direction and the bundle's mean direction. We also define the differential azimuthally dependent $\theta_{\text{eff}}(\phi)$ calculated by only including axon segments oriented between $\phi \pm \Delta\phi/2$, where we choose $\Delta\phi = 12°$.

The above definition in terms of $\cos\theta$ is also convenient in matching the spherical harmonics (SH)-based dMRI models (Anderson 2005; Dell'Acqua et al. 2007; Frank 2002; Jespersen et al. 2007, 2010, 2017; Novikov et al. 2018c;

Reisert et al. 2017; Tournier et al. 2007), where the diffusion signal is modeled in $3d$ by the convolution of a single-fiber segment's signal kernel with the FOD

$$\mathcal{P}(\hat{\boldsymbol{n}}) \simeq 1 + \sum_{l=2,4,\ldots} \sum_{m=-l}^{l} p_{lm} Y_{lm}(\hat{\boldsymbol{n}}) \,, \tag{2}$$

decomposed in the SH basis $Y_{lm}(\hat{\boldsymbol{n}})$, where p_{lm} are the SH coefficients. The rotational invariants p_l are determined by the 2-norm of SH coefficients via (Novikov et al. 2018c; Reisert et al. 2017)

$$p_l^2 = \frac{1}{\mathcal{N}_l^2} \sum_{m=-l}^{l} |p_{lm}|^2, \quad \mathcal{N}_l = \sqrt{4\pi(2l+1)}. \tag{3}$$

The normalization factor $\mathcal{N}_l$ is chosen such that $p_0 \equiv 1$ and $p_l \in [0,\ 1]$ for $l > 0$. The FOD of axon segments is contributed only by even orders l, since the FOD has an antipodal symmetry. A convenient rotationally invariant measure of the dispersion angle θ_{p_2} was given by (Novikov et al. 2018c)

$$\theta_{p_2} \equiv \cos^{-1} \sqrt{\langle \cos^2 \theta_i \rangle_{p_2}} \,, \tag{4a}$$

where

$$\langle \cos^2 \theta_i \rangle_{p_2} \simeq \frac{2p_2 + 1}{3} \,. \tag{4b}$$

This measure was inspired by the observation that for an axially symmetric FOD in the fiber basis (z-axis along the mean direction), its only non-zero SH coefficients are p_{l0}; the 2nd-order SH $p_{20} = \mathcal{N}_2 \cdot \left(3\left\langle \cos^2\theta \right\rangle - 1\right)/2$ is given in terms of the 2nd-order Legendre polynomial averaged over the FOD. As the norm of SH coefficients for a given l is basis-independent, the above definition of θ_{p_2} can be computed in any basis. Its added value is that the invariants p_l are directly estimated in the rotationally invariant framework for the "Standard Model" (Novikov et al. 2018c; Reisert et al. 2017). The value of θ_{p_2} coincides with θ_{eff} for axially symmetric FOD, and is practically close for single-fiber populations with relatively weak axial asymmetry, since both of their definitions are related with the rms of $\cos\theta_i$.

We note that (Reisert et al. 2017) proposed an empirical power-law functional form for the axially symmetric FOD: $p_l = p_0 \cdot \lambda^l$ of the Poisson kernel, where $p_0 \equiv 1$, and $\lambda \in [0,\ 1]$ is a dispersion parameter. We tested the applicability of this Poisson kernel, which effectively corresponds to the multipole expansion of a Coulomb potential.

Results

The IAS segmentations using RaW are compared to the ground-truth manual segmentation initialized by the ilastik Carving function for evaluating the accuracy of our method (Fig. 2). Next, quantifications of axonal size in mouse brain CC are reported, including size-related metrics (g-ratio, and inner, outer axonal diameter in Figs. 3, 4), orientation-related metrics (FOD in Fig. 5, dispersion angle and rotational invariants in Fig. 6), and their simulated time-dependence via coarse-graining for dMRI measurements.

RaW versus manual segmentation

Using RaW, we segmented the IAS of ~ 320 myelinated axons with ~ 59,000 cross sections in total. Furthermore, to validate RaW, we compared the segmentation results to a ground-truth consisting of 97 selected axons segmented manually with the initialization facilitated by the ilastik Carving function. The ground-truth IAS (Fig. 2a) covers the IAS entirely and includes the cytoplasm and organelles (also mitochondria attached to the myelin sheath by manual corrections). On the other hand, the IAS segmented using RaW (Fig. 2b) fails to cover organelles attached to the myelin sheath, since these structures are often considered as part of the myelin mask segmented using the pixelwise classifier.

The Jaccard index (Fig. 2d) and the Sørensen–Dice index (Fig. 2e) are the metrics to compare the IAS segmentations from the two methods. For most axons, both indices are high, manifesting the robustness of our random-hopping segmentation pipeline; this is also demonstrated by high values of similarity metrics in Table 1.

Table 1 Similarity metrics to compare IAS segmentations of the ground-truth and RaW

Similarity metric	IAS segmentations (ground-truth, RaW)
Jaccard index	0.85
Sørensen–Dice index	0.92
V^{rand}	0.68
V^{info}	0.89

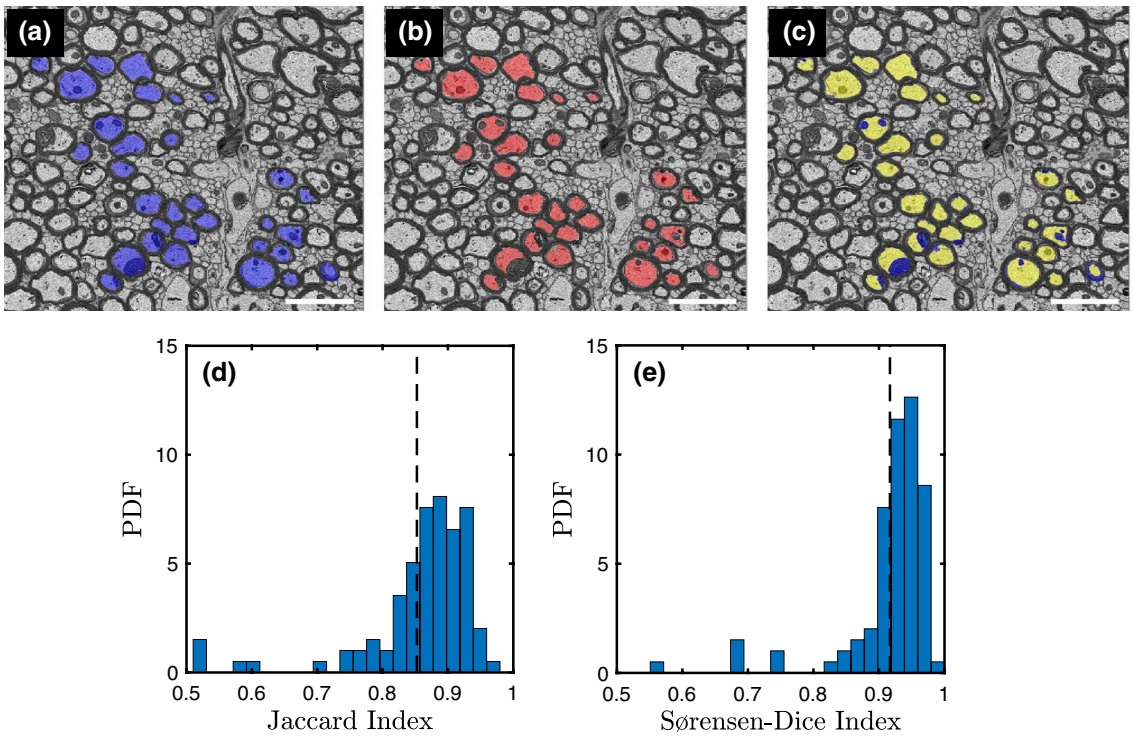

Fig. 2 IAS segmented **a** manually with the initialization facilitated by the ilastik Carving function (blue pixels), **b** using RaW (red pixels), and **c** the intersection of both methods (yellow pixels) in a representing slice. The histogram of the **d** Jaccard index and the **e** Sørensen–Dice index for the comparison of IAS segmentations from the two methods. The mean value is indicated by the dashed line. The scale bar in **a**–**c** is 4 µm

Inner axonal diameter

Table 2 and Fig. 8 in "Appendix B" illustrate how estimating the inner axonal diameter is significantly influenced by the choice of definition, such as the equivalent circle diameter, the short and long axis length of the fitted ellipse, and the inscribed circle diameter. The median of the inscribed circle diameter provides the smallest diameter estimates = 0.66 µm, and, in contrast, the mean of the long axis length provides the largest diameter estimates = 1.19 µm. The cross section perpendicular to the skeleton has an average eccentricity of 0.64 ± 0.15 (mean ± SD) and 0.65 (0.21) [median (Interquartile range, IQR)], indicating that axons are in general approximately elliptical, rather than circular or cylindrical.

Next, we used the equivalent circle diameter to evaluate the inner axonal diameter variation along each axon for diffusion times $t = [1, 10, 100]$ ms (Fig. 3a–c), along with the corresponding diameter histogram (Fig. 3d) (see "Inner axonal diameter", "Materials and methods" for details of diffusion smoothing kernel). At short diffusion times (Fig. 3a), the axonal diameter varies a lot within each axon, whereas at long diffusion times (Fig. 3c), axonal diameter variation is smoothed out within each axon. Therefore, the axonal diameter distribution at short diffusion times (blue curve in Fig. 3d) is slightly wider than that at long diffusion times (yellow curve in Fig. 3d).

Figure 3e shows the time-dependences of the average diameter $2\langle r\rangle$ and dMRI-sensitive effective diameter $2r_{\mathrm{eff}}$, where $r_{\mathrm{eff}}^4 \equiv \langle r^6\rangle / \langle r^2\rangle$ (Burcaw et al. 2015) is based on the signal attenuation in the wide-pulse limit (Neuman 1974), and $\langle \ldots \rangle$ denotes averaging over fiber segments of all axons. The mean diameter $2\langle r\rangle$ showed no obvious time-dependence (Fig. 3e); however, the dMRI-measured effective diameter $2r_{\mathrm{eff}}$, dominated by a sufficiently high-order moment of the distribution, showed significant time-dependence, ~ 17% change, for diffusion time t ranging over 1–100 ms.

g-Ratio

The histogram of the outer axonal diameter, inner axonal diameter, and the *g*-ratio are shown in Fig. 4a–c. Their mean ± SD is for the outer axonal diameter = 1.68 ± 0.45 µm, inner axonal diameter = 0.99 ± 0.42 µm, and *g*-ratio = 0.57 ± 0.09. For further comparisons with other studies, we also reported the median and the IQR in parenthesis for the outer axonal diameter = 1.61 (0.58) µm, inner axonal diameter = 0.90 (0.51) µm, and *g*-ratio = 0.57 (0.13).

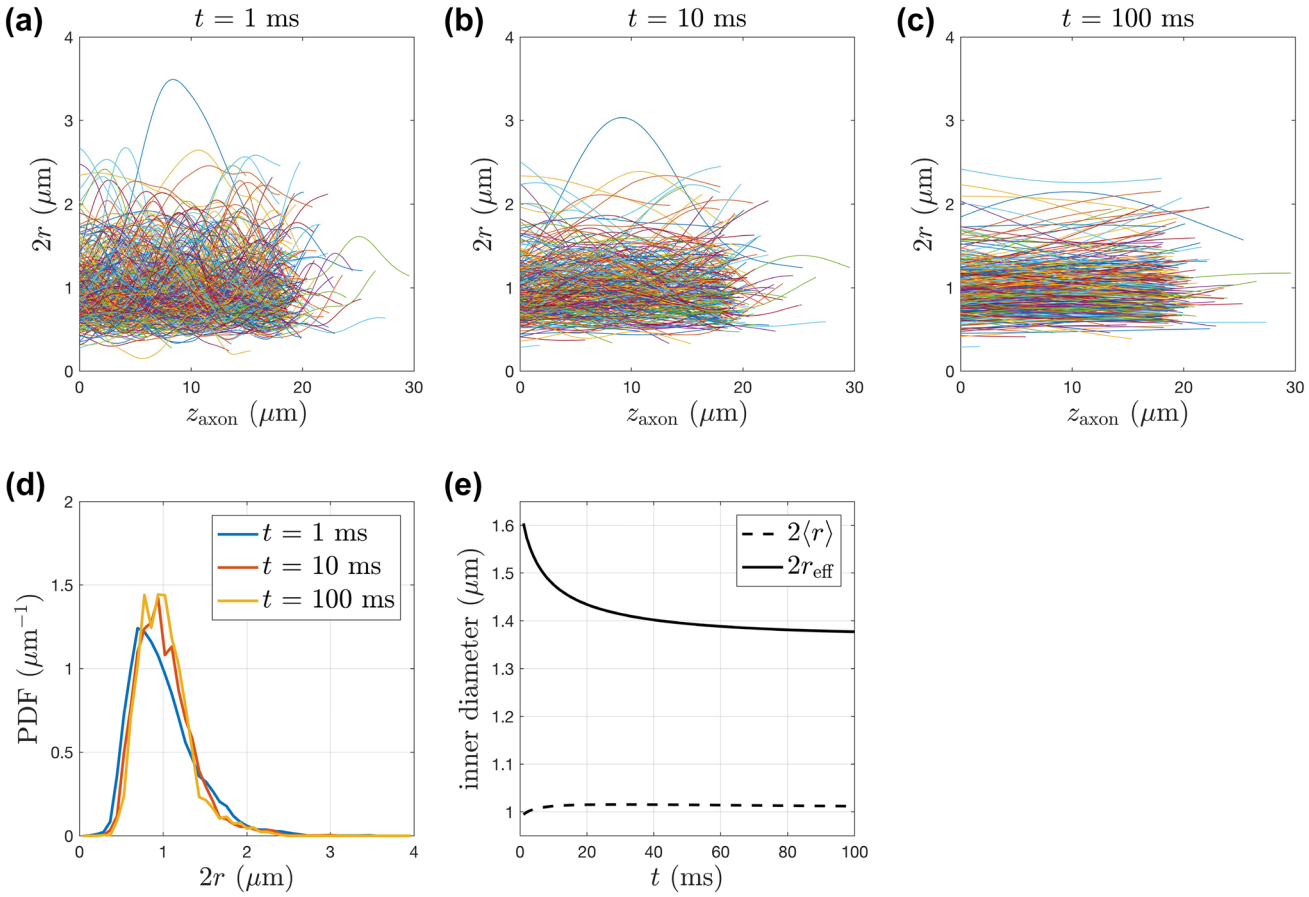

Fig. 3 Inner axonal diameter ($2r$) variation, estimated by the cross-sectional area perpendicular to the skeleton and displayed along the main direction of each axon (z_{axon}), was smoothed by a Gaussian kernel mimicking the diffusion process with an effective diffusion time $t =$ **a** 1 ms, **b** 10 ms, and **c** 100 ms. **d** Diameter histogram becomes narrower with longer diffusion time. **e** Average diameter $2\langle r\rangle$ has no significant time-dependence, whereas the dMRI-sensitive effective diameter $2r_{\text{eff}}$, where $r_{\text{eff}}^4 = \langle r^6\rangle / \langle r^2\rangle$ (Burcaw et al. 2015), has a non-trivial time-dependence for diffusion time $t < 50$ ms

The dependency of g-ratio on the inner diameter (Fig. 4d) is consistent with previous studies and fitted well by the reported log-linear functional form (Berthold et al. 1983; Little and Heath 1994; West et al. 2015), where the myelin sheath thickness is proportional to the number of myelin lamellae $n_l = C_0 + C_1 \cdot (2r) + C_2 \cdot \ln(2r)$. The fit in our data (red curve in Fig. 4d) has corresponding parameters $C_0 k = 0.35$ μm, $C_1 k = 0.006$, and $C_2 k = 0.024$ μm, where k is the myelin lamellar width (repeat distance).

The above estimated g-ratio values were obtained using a myelin thickness upper bound = 0.4 μm for the myelin sheath segmentation. However, the estimated myelin thickness and g-ratio could be biased by choosing an inappropriate upper bound value ("Appendix A", Fig. 7): a small upper bound could lead to a underestimated myelin thickness and an overestimated g-ratio, and vice versa.

In addition, the histogram of the along-axon variation of outer and inner axonal diameters is shown in Fig. 4e, f. Their mean ± SD is for the coefficient of variation of outer diameter = 0.17 ± 0.07, coefficient of variation of inner diameter = 0.28 ± 0.11. Their median (IQR) for the coefficient of variation of outer diameter = 0.16 (0.09), and coefficient of variation of inner diameter = 0.27 (0.16).

Fiber orientation distribution

The fiber skeleton was built based on the segmented IAS, with the fiber orientation calculated accordingly, and each axon's skeleton was smoothed and displayed with a 3d view angle (Fig. 5a) or a 2d projection (Fig. 5b) for $t = [1, 10, 100]$ ms. Longer diffusion time leads to a longer diffusion length and a wider smoothing kernel, and effectively smooths out each axon's tortuous skeleton. The FOD, displayed either on a triangulated spherical surface (Fig. 5c) or by a SH-constructed 3d glyph up to the order of $l = 10$ (Fig. 5d), indicates that longer diffusion time corresponds to a narrower fiber dispersion, which can be quantified by the dispersion angle in Fig. 6.

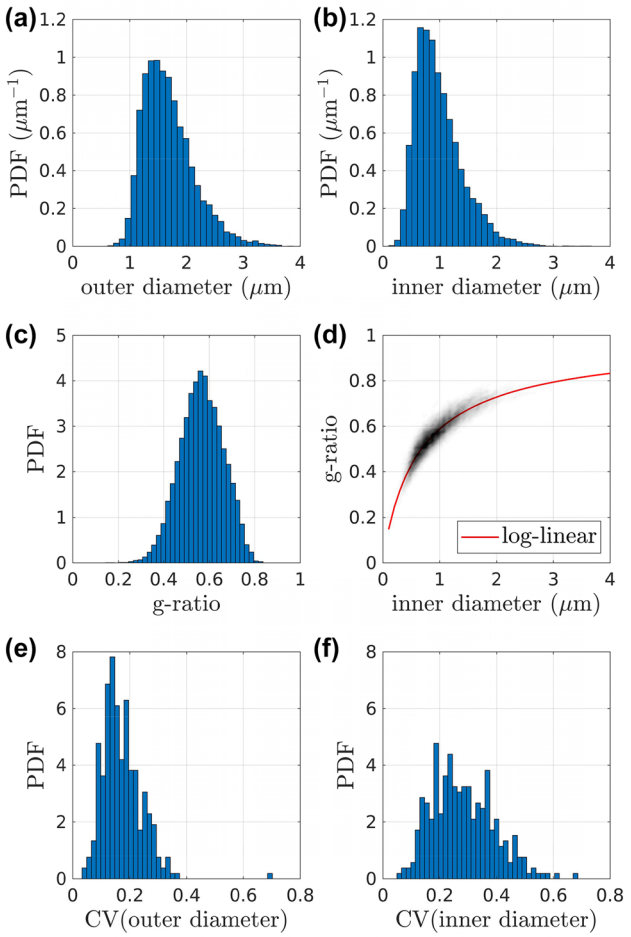

Fig. 4 Histogram of **a** outer axonal diameter, **b** inner axonal diameter, and **c** genuine *g*-ratio. The relation of *g*-ratio and inner diameter is shown in **d** as a 2*d* histogram, fitted by the log-linear equation (red curve) proposed by (Berthold et al. 1983). The histogram of **e** coefficient of variation (CV) of outer axonal diameter and **f** CV of inner axonal diameter show that axons are not perfect cylinders of CV (diameter) = 0

To compare with (Schilling et al. 2016) that applies a smoothing kernel of a 1 μm width, we also fitted the FOD of $t = 1$ ms ($\sigma = 1$ μm) to a Bingham distribution (Bingham 1974; Sotiropoulos et al. 2012), yielding fitting parameters $\kappa_1 = 19.2$ and $\kappa_2 = 4.5$. The orientation dispersion index, defined by (Mollink et al. 2017)

$$\mathrm{ODI}_{1,2} = \frac{2}{\pi}\tan^{-1}\left(\frac{1}{\kappa_{1,2}}\right),$$

is $\mathrm{ODI}_1 = 0.033$ and $\mathrm{ODI}_2 = 0.140$.

Dispersion angle and rotational invariants

As the orientation of each fiber segment was known, we estimated the dispersion angle observed in 2*d* histology (θ_{2d}) by projecting fiber segments on projection planes parallel to the main direction. The variation of the (cross-sectional) projected dispersion angle $\theta_{2d}(\phi)$ (Fig. 6a) and the effective dispersion angle $\theta_{\mathrm{eff}}(\phi)$ (Eq. (1), Fig. 6b) with respect to the azimuthal angle ϕ is hardly influenced by diffusion times $t = [1, 10, 100]$ ms. Generally, $\theta_{2d}(\phi)$ varies between 8° to 23°, and $\theta_{\mathrm{eff}}(\phi)$ varies between 6° to 31°.

Furthermore, we evaluated the dispersion angle of biophysical modeling of dMRI by analyzing the 3*d* orientation distribution of fiber segments (θ_{eff}) and its SH-based rotational invariants (θ_{p_2}, p_l). The time-dependence of rotational invariants (Eq. 3, Fig. 6c) is small for p_2 (3%), moderate for p_4 (11%), and large for p_6 (23%) for t ranging over 1–20 ms, and is small for p_2 (0.9%), p_4 (2.6%) and p_6 (4.7%) for diffusion time > 20 ms.

To further display the time-dependence of the dispersion angle, we calculated the averaged dispersion angle of the three definitions for t ranging over 1–100 ms in Fig. 6d, where the averaged θ_{2d} (rms of $\theta_{2d}(\phi)$ at $\phi = 1°, 2°, \ldots, 360°$) decreases with the diffusion time, from 18.2° ($t = 1$ ms, $\sigma = 1$ μm) to 16.8° ($t = 100$ ms, $\sigma = 10$ μm); the dMRI-sensitive dispersion angle θ_{eff} (Eq. 1), calculated using all axon segments, demonstrates a similar time-dependence, and is always larger than the corresponding histology-observed projected dispersion angle θ_{2d} for all diffusion times; the dispersion angle θ_{p_2} (Eqs. 4a, 4b), estimated by rotational invariants of the FOD, is slightly smaller than θ_{eff} and shows a similar time-dependence as well. The reason of $\theta_{p_2} \le \theta_{\mathrm{eff}}$ is that the FOD's axial asymmetry leads to contributions of $m \neq 0$ terms to p_2 values; therefore, $\langle \cos^2\theta_i \rangle_{p_2}$ is overestimated, and θ_{p_2} is underestimated, c.f. Eqs. (4a, 4b) and explanations right after. Generally, the time-dependence of dispersion angles (θ_{2d}, θ_{eff}, θ_{p_2}) is small ($\approx 1.7°$ for $t = 1$–100 ms) and negligible for diffusion time > 20 ms.

Rotational invariants seem to obey a power-law in a range of $l = 2, 4, \ldots, 10$ (Fig. 6e). However, this power-law behavior is not well-normalized and overshoots at $l = 0$. To compensate for that, a negative isotropic term needs to be introduced into the power-law, losing the simplicity of the Poisson kernel, that is

$$p_l \simeq C \cdot \lambda^l - (C-1)\delta_{0l}\,, \tag{5}$$

where C is a constant ≥ 1, and δ_{0l} is a Kronecker delta. In Fig. 6f, the dispersion parameters (λ, C) are obtained using a linear fit of $\log p_l$ with respect to $l = 2$–10. The base of the power-law is estimated via the slope $\log \lambda$, and the predicted p_0 is given by the intercept C at $l = 0$. By definition, $p_0 \equiv 1$; yet, this power-law relation ($\lambda \approx 0.8$) predicts a $p_0 > 1$, as manifested by an intercept C (≈ 1.1–1.2) > 1 at $l = 0$. The time-dependence of dispersion parameters is small (Fig. 6f) for λ (7%) and moderate for C (14%) for t ranging over 1–100 ms.

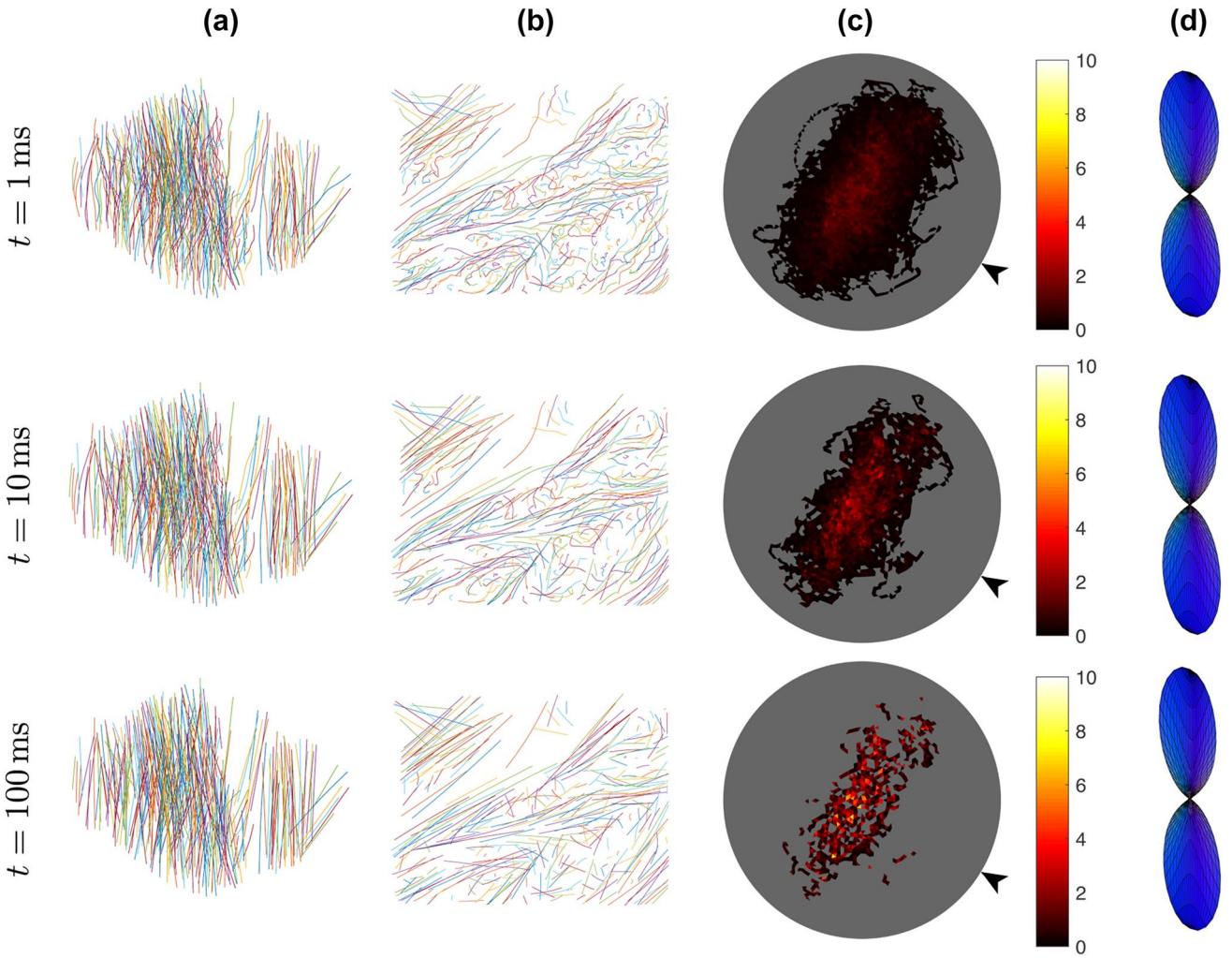

Fig. 5 **a** Skeleton of each segmented axon is smoothed to mimic the diffusion time-dependent coarse-grained microstructure along each axon's main direction with diffusion time $t = [1, 10, 100]$ ms. **b** Skeleton of each segmented axon in **a** was viewed from another view angle. Each axon becomes effectively straighter for longer diffusion times. **c** FOD of tangent vectors of all axon segments, starting at the center of a unit sphere, shows the intrinsic axonal dispersion. The unit of the colorbar is steradian^{-1}. **d** 3*d* FOD glyph was generated by fitting the FOD in **c** to spherical harmonics up to the order of $l = 10$. Arrows in **c** indicate the view angle for FOD glyphs in **d**

Discussion

Quantifying microstructural features from histology is essential for the validation of biophysical modeling. Here, we evaluated MRI-relevant metrics of brain white matter, via 3*d* high-resolution EM images, by quantifying the (inner) axon diameter, its distribution and variation along the axon, as well as the axonal dispersion, both in *2d* and *3d*. For that, we successfully segmented myelinated axons using a semi-automatic random-hopping-based algorithm. Effective diffusion time-dependence of the dMRI-relevant orientation-related and size-related tissue characteristics of the brain white matter microstructure is, for the first time, analyzed. The estimated dispersion angle of myelinated axons has negligible diffusion time-dependence at typical diffusion times observed with dMRI. In contrast, the estimated inner axonal diameter has a non-trivial time-dependence at diffusion times relevant for both pre-clinical and clinical diffusion imaging.

Here, we discuss our RaW algorithm as compared to a commonly used interactive segmentation tool, as well as how our results of size-related (*g*-ratio, inner axonal diameter) and orientation-related (FOD, dispersion angle, rotational invariants) tissue parameters compare to previous histological and MRI studies. Finally, we address some limitations of our methods.

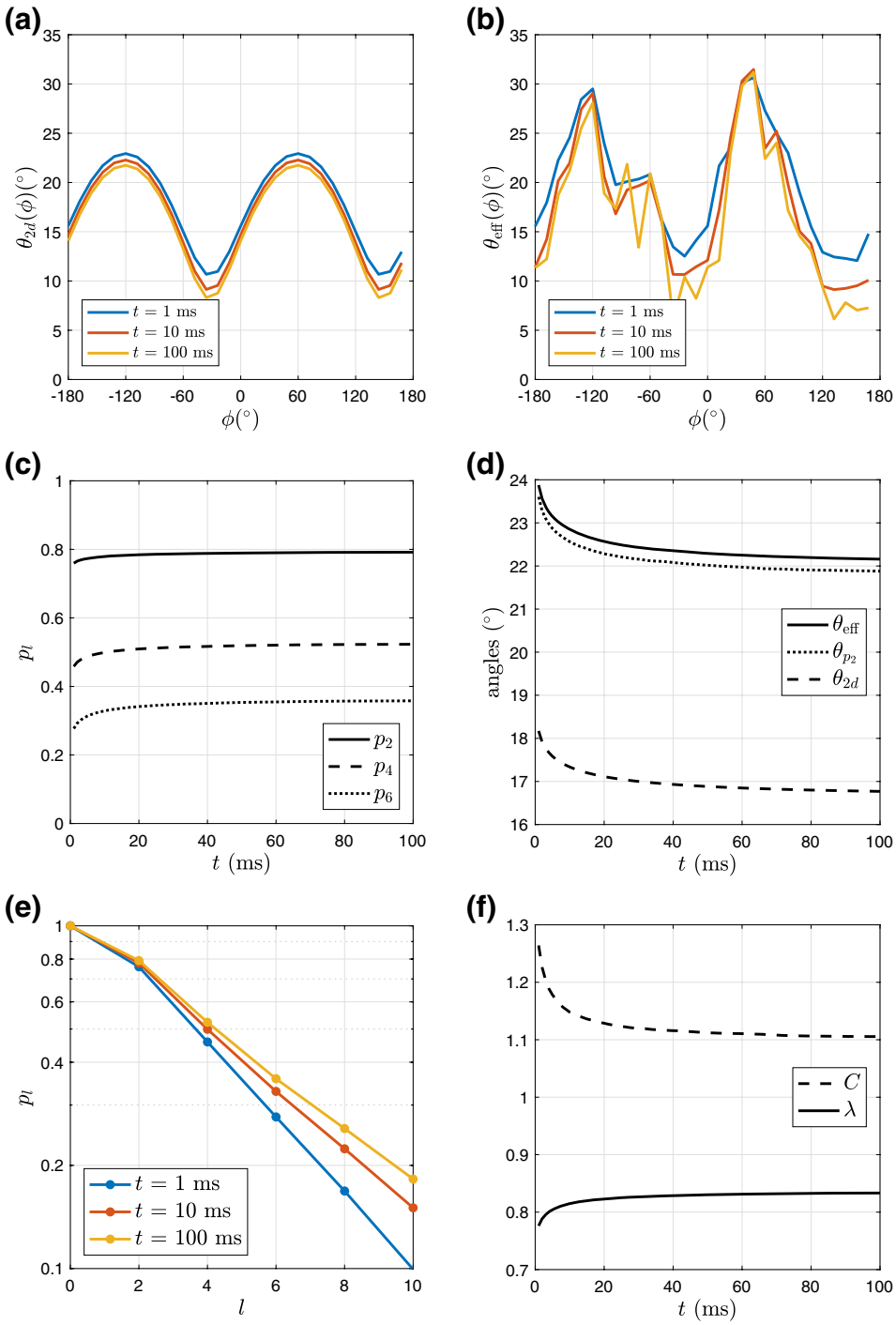

Fig. 6 **a** Projected dispersion angle $\theta_{2d}(\phi)$ and **b** dMRI-sensitive dispersion angle $\theta_{\text{eff}}(\phi)$ (Eq. 1), calculated within a bin width $\Delta\phi = 12°$, with respect to the azimuthal angle ϕ at diffusion time $t = [1, 10, 100]$ ms. **c** Rotational invariants $[p_2, p_4, p_6$ in Eq. (3)] show a small time-dependence for diffusion time $t = 20$–100 ms. **d** Dispersion angle averaged over all ϕ shows a time-dependence of $\approx 1.7°$ for diffusion time $t = 1$–100 ms. **e** Rotational invariants p_l with respect to the even orders $l = 2, 4, \ldots, 10$ at diffusion time $t = [1, 10, 100]$ ms. **f** Dispersion parameters of the modified power-law relation $[\lambda, C$ in Eq. (5)] obtained using a linear fit of $\log p_l$ with respect to $l = 2$–10 for diffusion time $t = 1$–100 ms

Segmentation methods (ground-truth and RaW)

Although ilastik greatly facilitates tracing of individual axons (one axon at a time), as in (Maco et al. 2014), it is still very labor-intensive to manually carve the segmentation. Each individual axon required much training data (object markers and background markers) in multiple slices, and the segmentation results change dynamically, while new markers are added, increasing the load of proofreading.

In contrast, our RaW algorithm is straightforward, and depends solely on the quality of the binary myelin mask. An imperfect myelin mask results in a segmentation (random-hopping trajectory) infiltrating into other axons or compartments, such as extra-axonal space. In this study, we successfully segmented ~70% of axons crossing the central slice, while the other ~30% of axons were deleted by the proofreading because of a leaky myelin mask. Our random-hopping-based method minimizes the need of manual seeding

Table 2 Inner axonal diameter of myelinated axons, calculated by the equivalent circle diameter (cross-sectional area), the short axis length and the long axis length of the fitted ellipse, and the inscribed circle diameter

	Inner axonal diameter (μm)	
	Mean (SD)	Median (IQR)
Equivalent circle diameter $=2\sqrt{\Omega/\pi}$	0.99 (0.42)	0.90 (0.51)
Short axis length	0.88 (0.38)	0.80 (0.47)
Long axis length	1.19 (0.50)	1.10 (0.63)
Inscribed circle diameter	0.74 (0.34)	0.66 (0.41)

Standard deviation (SD) and interquartile range (IQR) are shown in the parenthesis

and proofreading (e.g., 2 days, ~320 axons/person), reducing hard labor and simplifying the segmentation pipeline, e.g., 12 weeks, ~100 axons/person for the ground-truth. The manual seeding step can be further automated by extracting the regional maxima from the distance transform map of the myelin mask and the dilated edges (Abdollahzadeh et al. 2017). Confirmed with the ground-truth, RaW algorithm is robust and reliable to segment the IAS of myelinated axons. Mitochondria attached to the myelin sheath are deemed to be part of the myelin mask and, therefore, not delineated accurately, though it should be possible to separately identify the mitochondria using the semi-automatic pipeline incorporating the superpixel-based simple-linear-iterative-clustering (SLIC) method (Abdollahzadeh et al. 2017; Achanta et al. 2012).

One potential use of RaW is for machine-learning-based segmentation methods, where it is time-consuming to produce training, development, and test data set from 3*d* EM data. Using RaW method, we can rapidly generate enough data to train and validate other segmentation algorithms.

Inner axonal diameter distribution and along-axon variation

In this study, we first investigated the effect of different definitions of axonal diameters. While we used the equivalent circle diameter to evaluate inner and outer axonal diameters and the genuine *g*-ratio, the inner axonal diameter can also be estimated by other definitions, such as short and long axis length of the fitted ellipse, and the inscribed circle diameter (Table 2). In general, median diameters are smaller than mean diameters by 8–11%; compared with the equivalent circle diameter, the short axis length is smaller by ~11%, the long axis length is larger by ~21%, and the inscribed circle diameter is smaller by ~26%. The inscribed circle diameter was used as a diameter estimate in many histology studies (Aboitiz et al. 1992; Caminiti et al. 2009; Liewald et al. 2014), while some studies, on the other hand, did not mention their calculation methods of inner diameters. Hence, to unbiasedly compare diameter estimates between different studies, it is essential to clarify the definition used for diameter quantifications.

Compared to previous EM studies in mouse brain genu of CC, our inner diameter estimates (equivalent circle diameter) are larger by a factor of 1.1–2: 0.47 μm for 45-day-old mice in Sturrock (1980), 0.88 μm for > 18-week-old mice in Mason et al. (2001), 0.56 μm for adult mice in West et al. (2015) (age not specified), and 0.54 μm for an 8-week-old mouse in Sepehrband et al. (2016a). This is potentially caused by differences in calculation methods (e.g., equivalent circle diameter, short axis length, and inscribed circle diameter) and the image quality.

Furthermore, it is of interest to consider the inner axon diameter distribution. Indeed, although the Gamma distribution is the most commonly used, the generalized extreme value (GEV) distribution was previously found to describe the diameter distribution better (Sepehrband et al. 2016a). This argument also holds in our data for the inner diameter distribution shown in Figs. 4b (fits to distributions are shown in "Appendix B" and Fig. 8), implying that the assumption of Gamma distribution may oversimplify the realistic distribution of inner axonal diameters.

To evaluate the dMRI modeling assumption of perfectly straight cylindrical axons, we calculated the along-axon coefficient of variation of inner (≈ 0.3) and outer (≈ 0.2) diameters. Our findings indicate that the diameter variation is not negligible, as reported before in (Perge et al. 2009; Tang-Schomer et al. 2012) and very recently in (Abdollahzadeh et al. 2017; Marzan et al. 2018). This observation, as well as the non-zero eccentricity of the axonal cross section, suggest that the assumption of perfectly cylindrical axons may be too simplistic for modeling dMRI in brain.

To further understand this assumption, as well as understand the effect of diffusional coarse-graining, we studied the diffusion time-dependence, and found that the MRI-sensitive effective diameter $2r_{\mathrm{eff}}$ varies from 1.60 to 1.38 μm for $t = 1$–100 ms (Fig. 3e), showing that longer diffusion times leads to smaller estimates of the effective diameter $2r_{\mathrm{eff}}$ as measured by dMRI. This non-trivial time-dependence of $2r_{\mathrm{eff}}$ rejects the assumption of axonal shapes in perfect cylinders, which would imply no time-dependence of MRI-sensitive diameters. Our reported values of $2r_{\mathrm{eff}}$ are slightly larger than values in a previous histological study (1.32 μm) (Sepehrband et al. 2016b). However, in previous MRI literature, the dMRI-measured diameter is larger than our $2r_{\mathrm{eff}}$ estimation by a factor of ≥ 1.4, even when applying very strong diffusion-sensitive gradients $|\boldsymbol{g}| \leq 1350$ mT/m (Sepehrband et al. 2016b). This discrepancy could be due to neglecting the diffusion time-dependence of the extra-axonal signal (Burcaw et al. 2015; De Santis et al. 2016; Fieremans et al. 2016; Lee et al. 2017), i.e., potentially due to

misinterpreting the extra-axonal signal change as the intra-axonal one. Furthermore, when applying strong diffusion gradients, the dMRI-measured diameter is further biased by neglecting the higher order $|\boldsymbol{g}|^4$ corrections (Lee et al. 2017) to the intra-axonal model in (Neuman 1974).

g-Ratio

We measured a relatively smaller histology *g*-ratio value ≈ 0.6, as compared to previous histological studies: 0.808 for > 18-week-old mice (Mason et al. 2001), 0.81 for adult mice (West et al. 2015) (age not specified), and 0.76 for 2-month-old mice (Yang et al. 2016). This could be caused by (1) the difference of changes in myelin structures during the EM processing (Kirschner and Hollingshead 1980), such as fixation and dehydration, and (2) potentially inaccurate segmentation of the myelin sheath. Since we only segmented some axons, instead of all, the watershed algorithm cannot avoid overestimation of the segmented myelin sheath, which touches the myelin sheath of the unsegmented axons, leading to an overall overestimated myelin sheath thickness and a slightly underestimated *g*-ratio in our study.

Different definitions of *g*-ratio are used in the field of histology versus MRI, with the latter (g_{MRI}) sometimes being called the aggregate *g*-ratio, as defined by $g_{\mathrm{MRI}} = \sqrt{1 - \mathrm{MVF}/\mathrm{FVF}}$ (Stikov et al. 2011), where MVF and FVF are the myelin volume fraction and the fiber volume fraction, respectively. However, while MRI models typically assume a single *g*-ratio value for the axons within an MRI voxel, we reported that the genuine *g*-ratio *g* from histology has a non-negligible variation over our sample size (Fig. 4c) which is much smaller than a typical MRI voxel (by an order of 100). to compare MRI measurement with histology, (West et al. 2016) proposed the following relation between the g_{MRI} and the genuine histology *g*:

$$g_{\mathrm{MRI}}^2 = \frac{\left\langle g^2 r'^2 \right\rangle}{\left\langle r'^2 \right\rangle},$$

which corresponds to an estimated $g_{\mathrm{MRI}} = 0.61$ in this study, in agreement with the aggregate *g*-ratio = 0.62 for rat brain CC in (Abdollahzadeh et al. 2017) and aggregate *g*-ratio = 0.69 for macaque brain CC in (Stikov et al. 2015).

FOD, dispersion angle, and rotational invariants

Our study presents a 3*d* EM-based extraction of fiber dispersion in the mouse brain genu of CC, and reports good agreement with dispersion estimated using confocal microscopy and light microscopy. In particular, the FOD at $t = 1$ ms (smoothed by $\sigma = 1$ μm) fitted to a Bingham distribution suggests a κ_1 value ≈ 19, corresponding to small dispersion (e.g., single-fiber dispersion), consistent with existing literature ~ 21 (Schilling et al. 2016), where the structure tensor analysis was applied to 3*d* stacks of confocal microscopy images in monkey brains using a Gaussian kernel (standard deviation = 1 μm) to calculate spatial derivatives. In contrast, the κ_2 value ≈ 5 in this study, related to large dispersion (e.g., fiber fanning), is different from the previous study ~ 12 (Schilling et al. 2016), probably influenced by the sampling site in CC.

In addition, the estimated 2*d* dispersion angle θ_{2d} (Appendix C) is in agreement with previous 2*d* histological studies yielding a dispersion of ~ 18.1° for the human brain CC in (Ronen et al. 2014) and 17° for the rat brain CC in (Leergaard et al. 2010). Remarkably, the estimated 3*d* dispersion angle θ_{p_2} (Eqs. 4a, 4b) based on rotational invariant p_2 is also in agreement with the recently dMRI-estimated in vivo fiber dispersion ~ 26° in the human brain CC (Dhital et al. 2019; Novikov et al. 2018c; Veraart et al. 2018b). Along directions with small fiber spread ($\phi \approx -30°$ and 150° in Fig. 6a, b), the dispersion angle is $\approx 8°$ with $\mathrm{ODI}_1 = 0.033$, consistent with values estimated from confocal microscopy images of the CC (Schilling et al. 2018).

Theoretically, the 2*d* dispersion angle θ_{2d} is smaller than the 3*d* dispersion angle θ_{3d} (e.g., θ_{eff}, θ_{p_2}): For a fiber bundle with an axially symmetric FOD, the 2*d* and 3*d* dispersion angles are related via ("Appendix C")

$$\cos^2\theta_{2d} = \left\langle \left|\cos\theta_i\right| \right\rangle \simeq \cos\theta_{3d}. \tag{6}$$

For small dispersion angles, performing Taylor expansions for both sides of Eq. (6) leads to a simple relation $\theta_{2d} \simeq \theta_{3d}/\sqrt{2}$.

Although the estimated FOD of our sample is not in perfectly axial symmetry (Fig. 5), the estimated 2*d* dispersion angles (Fig. 6d) can still be predicted by 3*d* dispersion angles via Eq. (6) with 7% error (Fig. 9b). With the knowledge of FOD's rotational invariants p_l of even order l, we can estimate the 2*d* dispersion angle with only 3% error caused by a lack of perfect axial symmetry in our FOD ("Appendix C", Eq. (9), Fig. 9b). The above simple relations between 2*d* and 3*d* dispersion angles, as well as their relation to the counting problem and the Steiner compact discussed at the end of "Appendix C", help to compare recent studies (e.g., 3*d* histology, dMRI measurements) with previous 2*d* histological results.

Furthermore, the estimated dispersion angle is comparable between dMRI studies using different diffusion times, as we found the time-dependence of dispersion angles is minimal (~ 8% for $t = 1$–100 ms in Fig. 6d). Similarly, for diffusion time > 20 ms, the time-dependence of rotational invariants (p_2, p_4, p_6) is minimal (0.9–4.7% for $t = 20$–100 ms in Fig. 6c), confirming that the SH-based models estimate the genuine FOD shape, and the diffusional coarse-graining has negligible effects.

As initially proposed by Reisert et al. (2017), we verified that the rotational invariants approximately obey a power-law (Poisson kernel) of the order l for $l = 2$–10, and found that this power-law behavior is quite consistent, however it is not well-normalized and overshoots at $l = 0$ (Fig. 6e). The dispersion parameters (λ, C) defined in Eq. (5) are obtained using a linear fit of $\log p_l$ with respect to $l = 2$–10, whereby the fitted $C > 1$ indicates the overshoot of the power-law relation at $l = 0$ (Fig. 6f).

Limitations

This study has some limitations that may be addressed in future research. First, the random-hopping-based segmentation method (RaW) may be further improved, as it depends strongly on the quality of the myelin mask. In particular, mitochondria directly attached to the inner myelin border are sometimes recognized as part of the myelin mask and need to be separately identified by other algorithms (Abdollahzadeh et al. 2017; Achanta et al. 2012). In addition, while segmenting the individual myelin sheath for each axon, we assigned an upper bound for the myelin thickness (Kleinnijenhuis et al. 2017) to limit errors in our segmentation. This upper bound could influence the *g*-ratio estimation ("Appendix A", Fig. 7): a small upper bound leads to an under-segmented myelin sheath and a large *g*-ratio, and a large upper bound leads to an over-expanded myelin sheath and a small *g*-ratio. Determining the upper bound of the myelin thickness is crucial when evaluating the *g*-ratio and the actual myelin thickness.

Next, our EM sample is relatively small, as compared to those obtained from other imaging techniques, such as light microscopy (Grussu et al. 2016; Ronen et al. 2014), polarized light imaging (Mollink et al. 2017), and confocal microscopy (Schilling et al. 2016, 2018), and results based on EM segmentations could be less representative because of the limited field-of-view. Nonetheless, the size of our sample was large enough to study the effect of coarse-graining due to finite diffusion times as employed in dMRI, leading to relevant findings for interpreting this non-invasive imaging method.

Finally, in this study, we only focused on myelinated axons. Other structures, such as unmyelinated axons, astrocytes, microglia, and blood vessels, are also important and should be studied in further work to extend the current analysis.

Code sharing

The source codes of our segmentation pipeline and analysis tools can be downloaded on our github page (https://github.com/NYU-DiffusionMRI).

Conclusions

We quantified several axonal features related to the size and dispersion in a *3d* SEM sample of the genu CC of mouse brain. For that, we developed a random-hopping-based segmentation method facilitating a 3*d* EM segmentation pipeline in brain white matter, and estimated the inner and outer axonal diameter as well as the myelin *g*-ratio according to various definitions by analyzing the cross section perpendicular to the axon skeleton. Furthermore, non-trivial variations in inner and outer diameters are observed, implying that the assumption of perfectly cylindrical axons may be too simplistic for dMRI modeling of the brain. This is further confirmed by our estimate of diffusional coarse-graining, showing that the diffusion time-dependence of the dMRI-derived axon diameter metric is non-negligible, as it leads to narrowing of the effective axonal diameter distribution and to a decrease of the effective MRI-derived axonal diameter. Besides size-related metrics, the 3*d* EM segmentation provides an accurate and reliable evaluation of the fiber orientation dispersion, and the calculated projected dispersion angle is compatible with previous 2*d* histological studies. The estimated MRI-measurable dispersion angle from histology is found to agree with previous MRI studies, with a very small diffusion time-dependence.

Acknowledgements We would like to thank the NYULH DART Microscopy Lab Alice Liang, Kristen Dancel-Manning and Chris Patzold for their expertise in electron microscopy work, Kirk Czymmek and Pal Pedersen from Carl Zeiss for their assistance of 3*d* EM data acquisition, and Marios Georgiadis for the discussion of the myelin structure change caused by tissue preparations. It is also a pleasure to thank Markus Kiderlen from Aarhus University and Valerij Kiselev from University Medical Center Freiburg for a discussion on the relation between 2-dimensional and 3-dimensional axonal dispersions; Markus Kiderlen has also kindly provided the reference on the relation between the Steiner compact and the cosine transform of the FOD discussed in Appendix C. Jelle Veraart is a Postdoctoral Fellow of the Research Foundation - Flanders (FWO; grant number 12S1615N). Research was supported by the National Institute of Neurological Disorders and Stroke of the NIH under award number R21 NS081230 (Fieremans, E., Novikov, D. S., and Kim, S. G.) and R01 NS088040 (Fieremans, E. and Novikov, D. S.), and was performed at the Center of Advanced Imaging Innovation and Research (CAI2R, http://www.cai2r.net), an NIBIB Biomedical Technology Resource Center (NIH P41 EB017183, Fieremans, E., Novikov, D. S., and Kim, S. G.).

Funding This study was supported by the National Institute of Neurological Disorders and Stroke of the NIH under award number R21 NS081230 (Fieremans, E., Novikov, D. S., and Kim, S. G.) and R01 NS088040 (Fieremans, E. and Novikov, D. S.), and was performed at the Center of Advanced Imaging Innovation and Research (CAI2R, http://www.cai2r.net), an NIBIB Biomedical Technology Resource Center (NIH P41 EB017183, Fieremans, E., Novikov, D. S., and Kim, S. G.).

Compliance with ethical standards

Conflict of interest The authors declare that they have no conflict of interest.

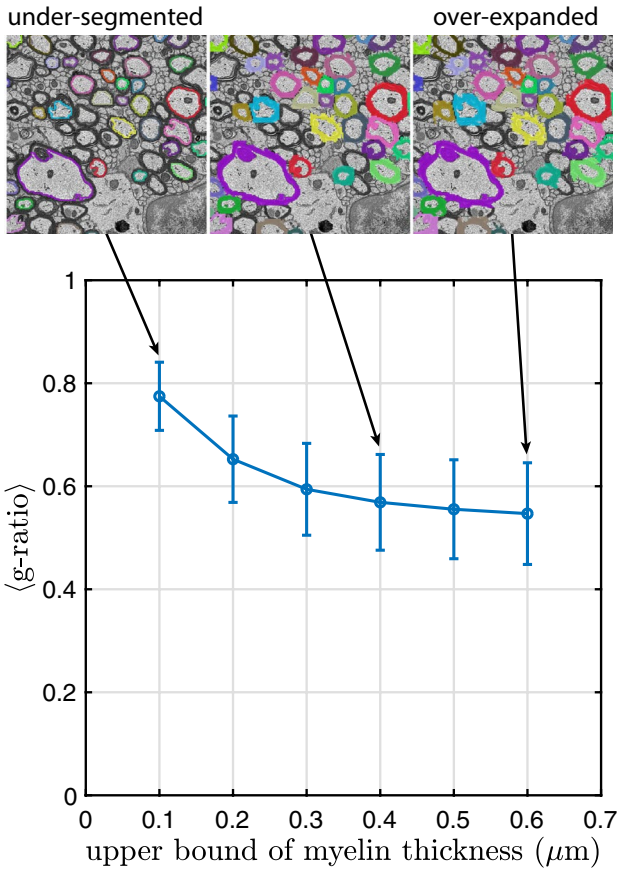

Fig. 7 Artificial upper bound applied for myelin sheath segmentation influences the estimated mean *g*-ratio. A small upper bound for the myelin thickness leads to under-segmented individual myelin sheaths (top left, upper bound = 0.1 μm). In contrast, a large upper bound causes over-expanded individual myelin sheaths (top right, upper bound = 0.6 μm). In this study, an upper bound of 0.3–0.4 μm results in appropriate individual myelin sheaths (top middle, upper bound = 0.4 μm)

Ethical approval All procedures performed in studies involving animals were in accordance with the ethical standards of New York University School of Medicine. All mice were treated in strict accordance with guidelines outlined in the National Institutes of Health Guide for the Care and Use of Laboratory Animals, and the experimental procedures were performed in accordance with the Institutional Animal Care and Use Committee at the New York University School of Medicine. This article does not contain any studies with human participants performed by any of the authors.

Informed consent Not applicable.

Appendix A: The myelin thickness upper bound used for the segmentation could influence *g*-ratio estimations

The estimated *g*-ratio values could be influenced by the myelin thickness upper bound used for dilating the segmented IAS to further segment the myelin sheath ("Myelin sheath and *g*-ratio", "Materials and methods"). In Fig. 7, six different upper bound values, varying from 0.1 to 0.6 μm, are used to segment the myelin sheath and calculate the mean *g*-ratio, ranging from 0.77 to 0.55, indicating that the upper bound has to be carefully chosen for an accurate *g*-ratio estimation. A small upper bound (e.g., Fig. 7, upper left) could lead to a underestimated myelin thickness and an overestimated *g*-ratio; in contrast, a large upper bound (e.g., Fig. 7, upper right) could lead to an overestimated myelin thickness and a underestimated *g*-ratio.

Appendix B: Axonal diameter estimates per various definitions

In this section, distributions of axonal diameters are shown based on different definitions, such as equivalent circle diameter (Fig. 8a), short and long axis length of the fitted ellipse (Fig. 8b, c), and inscribed circle diameter (Fig. 8d). To compare with a previous study (Sepehrband et al. 2016a), we fitted the axonal diameter histogram to Gamma distribution and generalized extreme value (GEV) distribution in Fig. 8, which shows that GEV distribution fits better to the experimental diameter distribution (of all four definitions) than Gamma distribution does, consistent with the conclusion in (Sepehrband et al. 2016a). Also, GEV distribution has a longer tail than Gamma distribution does for thick axons in diameters > 3–5 μm, manifested by semi-logarithmic plots of diameter distributions in the bottom row of Fig. 8.

Appendix C: Relations between 2*d* and 3*d* dispersion angles

The purpose of this Appendix is to relate the 2*d* dispersion angle θ_{2d} derived from 2*d* histology (using, e.g., structure tensor) to the 3*d* dispersion angle θ_{3d} (defined, e.g., as θ_{eff} or θ_{p_2} in the main text). It is quite obvious that, generally, $\theta_{2d} \leq \theta_{3d}$, since the projection onto a plane removes part of the orientational variance (in the direction transverse to that plane). Here we address this relation quantitatively, and also estimate the 2*d* dispersion angle in terms of the 3-dimensional FOD's SH coefficients and rotational invariants.

Aligning the *z*-axis with the main direction of a fiber bundle, the *i*-th fiber segment is defined by the polar and azimuthal angles (θ_i, ϕ_i). Its 2*d* projection angle $\theta_i' = \theta_i'(\theta_i, \phi_i)$ within a

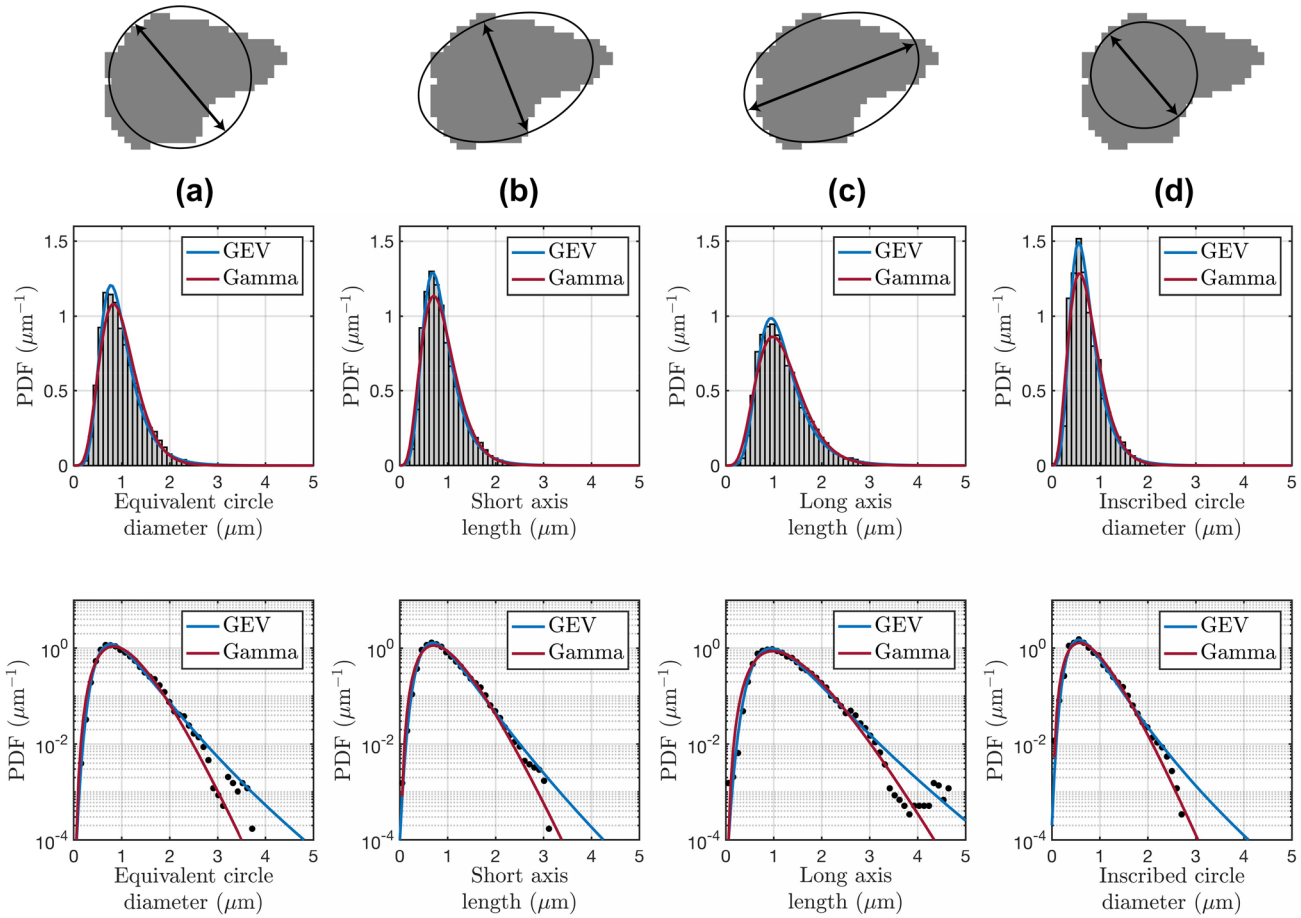

Fig. 8 Distribution of axonal diameters, defined by **a** equivalent circle diameter calculated from the cross-sectional area, **b** short axis length and **c** long axis length of the fitted ellipse, and **d** inscribed circle diameter. The upper row shows an exemplified axon cross section (gray area) and the corresponding diameter estimates (double-arrowed lines). The middle row shows experimental diameter distributions (gray bars) and the fits based on the Gamma distribution (red) and the generalized extreme value distribution (GEV) (blue). The bottom row is the middle row displayed in a semi-logarithmic scale for experimental data (data points) and the fits (solid lines)

plane (e.g., x–z plane in Fig. 9a) parallel to the main direction (z-axis), can be determined as

$$\cos\theta_i' = \frac{z}{\sqrt{x^2+z^2}} = \frac{\cos\theta_i}{\sqrt{\sin^2\theta_i\cos^2\phi_i + \cos^2\theta_i}}\,.$$

We now define the $2d$ dispersion angle. One can average the above θ_i' over the FOD,

$$\theta_{2d}^2 \equiv \langle \theta_i'^2 \rangle,$$

such that

$$\cos^2\theta_{2d} = \cos^2\sqrt{\langle\theta_i'^2\rangle} \simeq 1 - \langle\theta_i'^2\rangle \simeq \langle\cos^2\theta_i'\rangle,$$

or, alternatively, adopt the above Taylor approximation as a definition, since it is actually more natural to average $\cos^2\theta_i'$ rather than the angle itself, as $\cos^2\theta_i'$ corresponds to the structure tensor component.

The FOD average will be performed in two steps. First, we average $\cos^2\theta_i'$ over the azimuthal angle ϕ_i. This can be explicitly done if the FOD is axially symmetric. We also note that random histological sampling performed on a sufficiently large scale effectively performs such azimuthal averaging. The azimuthal averaging can be performed exactly for any fixed θ_i:

$$\langle\cos^2\theta_i'\rangle_{\phi_i} \equiv \int_0^{2\pi} \cos^2\theta_i' \frac{d\phi_i}{2\pi} = \left|\cos\theta_i\right|. \tag{7}$$

Hence, we explicitly see that the azimuthal $2d$ dispersion variance is given by the first power of $\cos\theta_i$, which is greater than the $3d$ variance $\cos^2\theta_i$, corresponding to a narrower $2d$ dispersion, $\theta_{2d} \leq \theta_{3d}$, cf. Equation (6) of the main text.

At the second step, we average Eq. (7) over the remaining polar angle θ_i to obtain $\cos^2\theta_{2d} = \langle|\cos\theta_i|\rangle$. We can already

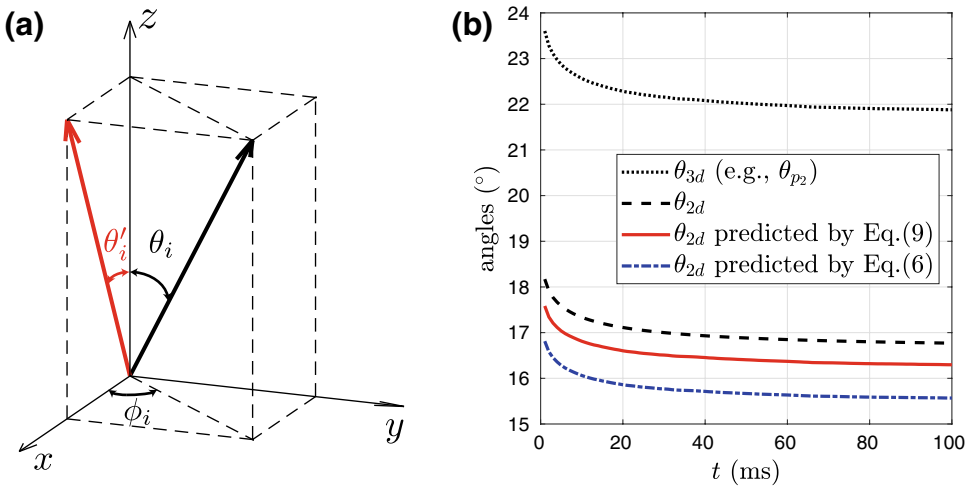

Fig. 9 **a** Considering a fiber bundle with its main direction aligned to the z-axis, the $3d$ dispersion angle θ_{3d} is defined by the fiber segment (black) orienting into (θ_i, ϕ_i) in $3d$ space, and the $2d$ dispersion angle θ_{2d} is defined by the fiber segment projection (red) on a $2d$ plane (e.g., x–z plane) with a $2d$ projection angle θ_i'. **b** The $3d$ dispersion angle (e.g., θ_{p_2} in Eqs. 4a, 4b) is larger than the $2d$ dispersion angle as in Fig. 6d. The prediction of $2d$ dispersion angle based on FOD's rotational invariants up to the order $l=20$, Eq. (9) (red solid line), has a 3% error. Similarly, the prediction based on the $3d$ dispersion angle (e.g., θ_{p_2}), Eq. (6) (blue dash–dotted line), has a 7% error. These errors are potentially caused by the axial asymmetry in our FOD, as shown in Fig. 5

see that for narrow FODs, Taylor-expanding up to $\langle \theta_i^2 \rangle \simeq \theta_{3d}^2$, we find $\theta_{2d} \simeq \theta_{3d}/\sqrt{2}$, which is just a statement that the variance of the axial radius $\langle x^2 + y^2 \rangle = 2\langle x^2 \rangle$ is given by twice the variance of its x- or y-coordinate. Note, however, that this approximation ceases to be correct for the higher orders of θ, essentially because of the non-trivial denominator $\sqrt{x^2+z^2}$ in the definition of $\cos\theta_i'$, as opposed to $\sqrt{x^2+y^2+z^2}=1$.

To estimate the $2d$ dispersion angle based on FOD's SH coefficients p_{lm} in Eq. (2), we average the right-hand side of Eq. (7), where only the $m=0$ SH contribute due to the axial symmetry. Using Eq. (2) and $Y_{l0}(\theta) = \sqrt{\frac{2l+1}{4\pi}} P_l(\cos\theta)$, where $P_l(\cos\theta)$ are the Legendre polynomials, we obtain

$$\begin{aligned} \cos^2\theta_{2d} \simeq \langle \cos^2\theta_i' \rangle &= \int_{-1}^{1} |\cos\theta_i| \mathcal{P}(\hat{\boldsymbol{n}}) \cdot \frac{1}{2} d(\cos\theta_i) \\ &= \frac{1}{2} + \sum_{l=2,4,\ldots}^{\infty} p_{l0} \cdot \sqrt{\frac{2l+1}{4\pi}} \cdot \int_0^1 z\, P_l(z)\, \mathrm{d}z\,, \end{aligned} \tag{8}$$

where the integral

$$\int_0^1 z\, P_l(z)\, \mathrm{d}z = \frac{(-1)^{l/2+1}}{(l-1)(l+2)} \cdot \frac{(l-1)!!}{l!!}\,, \qquad l = 2, 4, \ldots$$

can be evaluated using the generating function of Legendre polynomials $\frac{1}{\sqrt{1-2tz+t^2}} = \sum_l P_l(z) t^l$, such that $\int_0^1 \frac{z}{\sqrt{1-2tz+t^2}}\,\mathrm{d}z = \int_{-\infty}^{\infty} \frac{\mathrm{d}\lambda}{\sqrt{\pi}} \int_0^1 z\mathrm{d}z\, \mathrm{e}^{-\lambda^2(1-2tz+t^2)}$ and the subsequent integral is reduced to a few Euler's Gamma functions.

Finally, we use the definition in Eq. (3) to express p_{l0} via the rotational invariants p_l, when the other $m \neq 0$ FOD harmonics are either zero (axial symmetry) or negligible. As a result, we find

$$\cos^2\theta_{2d} \simeq \frac{1}{2} + \sum_{l=2,4,\ldots}^{\infty} p_l \cdot \frac{(-1)^{l/2+1}\,(2l+1)}{(l-1)(l+2)} \cdot \frac{(l-1)!!}{l!!}\,. \tag{9}$$

It is important to note that the $2d$ dispersion angle θ_{2d} appears to depend on the SH and rotational invariants p_l with all l, in contrast to the $3d$ dispersion angle $\cos^2\theta_{3d} = (2p_2+1)/3$ in Eqs. (4a, 4b), which only involves the irreducible representation of the SO(3) group of rotations with the weight $l=2$. It is quite obvious that the $3d$ definition of the dispersion angle is more natural (after all, the FOD is a 3-dimensional object), and mathematically, it is a better quantity, since it only depends on the $l=2$ invariant, and does not mix the irreducible representations of SO(3). The above equation gives the precise way to compare $2d$ and $3d$ FOD estimates.

Figure 9b shows that the predicted $2d$ dispersion angle based on rotational invariants and Eq. (9) is close to the value calculated by projecting fiber segments on $2d$ planes, with only 3% error due to a lack of perfect axial symmetry of our FOD.

We note that Eq. (7) derived above has an interesting geometric meaning. Its right-hand side, averaged over the FOD, provides the cosine transform of the FOD [cf. Eq.(8) above], with respect to the z-axis. We now recall that the cosine transform of the FOD, multiplied by the length-to-volume ratio of all fiber segments, equals to the number density of intersections of the fibers by the x–y plane. This statement is intuitively obvious (fiber length projected onto the z-axis contributes to the intersection); it is rigorously discussed for the point processes, e.g., in Eq. (4.40) of the book (Schneider and Weil 2008). This statement is valid in any basis, and serves as a foundation for constructing the Steiner compact, which is an equivalent FOD representation. In other words, the FOD, whose direct estimation relies on calculating the gradients to determine the local directions, through the cosine transform is related to a simpler, counting problem, of calculating the numbers of intersections by all possible planes. Going back from the Steiner compact to the FOD by inverting the cosine transform is essentially rederived above, cf. the right-hand side of Eq. (9). Remarkably, we can see that the left-hand side of Eq. (7) relates the Steiner compact to the structure tensor calculation in the x–z plane. This means that the angular-averaged $2d$ structure tensor calculation (in any plane parallel to z) can also be performed as a counting problem, by counting the density of fiber intersections by the plane orthogonal to z.

References

Abdollahzadeh A, Belevich I, Jokitalo E, Tohka J, Sierra A (2017) 3D axonal morphometry of white matter. https://doi.org/10.1101/239228

Aboitiz F, Scheibel AB, Fisher RS, Zaidel E (1992) Fiber composition of the human corpus callosum. Brain Res 598:143–153

Achanta R, Shaji A, Smith K, Lucchi A, Fua P, Susstrunk S (2012) SLIC superpixels compared to state-of-the-art superpixel methods. IEEE Trans Pattern Anal Mach Intell 34:2274–2282. https://doi.org/10.1109/TPAMI.2012.120

Adams R, Bischof L (1994) Seeded region growing. IEEE Trans Pattern Anal 16:641–647

Alexander DC, Hubbard PL, Hall MG, Moore EA, Ptito M, Parker GJ, Dyrby TB (2010) Orientationally invariant indices of axon diameter and density from diffusion. MRI Neuroimage 52:1374–1389. https://doi.org/10.1016/j.neuroimage.2010.05.043

Arganda-Carreras I et al (2015) Crowdsourcing the creation of image segmentation algorithms for connectomics. Front Neuroanat 9:142. https://doi.org/10.3389/fnana.2015.00142

Anderson AW (2005) Measurement of fiber orientation distributions using high angular resolution diffusion imaging. Magn Reson Med 54(5):1194–1206

Assaf Y, Basser PJ (2005) Composite hindered and restricted model of diffusion (CHARMED) MR imaging of the human brain. Neuroimage 27:48–58. https://doi.org/10.1016/j.neuroimage.2005.03.042

Assaf Y, Blumenfeld-Katzir T, Yovel Y, Basser PJ (2008) AxCaliber: a method for measuring axon diameter distribution from diffusion MRI. Magn Reson Med 59:1347–1354. https://doi.org/10.1002/mrm.21577

Barazany D, Basser PJ, Assaf Y (2009) In vivo measurement of axon diameter distribution in the corpus callosum of rat brain. Brain 132:1210–1220. https://doi.org/10.1093/brain/awp042

Benjamini D, Komlosh ME, Holtzclaw LA, Nevo U, Basser PJ (2016) White matter microstructure from nonparametric axon diameter distribution mapping. Neuroimage 135:333–344. https://doi.org/10.1016/j.neuroimage.2016.04.052

Berthold CH, Nilsson I, Rydmark M (1983) Axon diameter and myelin sheath thickness in nerve fibres of the ventral spinal root of the seventh lumbar nerve of the adult and developing cat. J Anat 136:483–508

Bingham C (1974) Antipodally symmetric distribution on sphere. Ann Stat 2:1201–1225

Budde MD, Frank JA (2010) Neurite beading is sufficient to decrease the apparent diffusion coefficient after ischemic stroke. Proc Natl Acad Sci USA 107:14472–14477. https://doi.org/10.1073/pnas.1004841107

Burcaw LM, Fieremans E, Novikov DS (2015) Mesoscopic structure of neuronal tracts from time-dependent diffusion. Neuroimage 114:18–37. https://doi.org/10.1016/j.neuroimage.2015.03.061

Caminiti R, Ghaziri H, Galuske R, Hof PR, Innocenti GM (2009) Evolution amplified processing with temporally dispersed slow neuronal connectivity in primates. Proc Natl Acad Sci USA 106:19551–19556. https://doi.org/10.1073/pnas.0907655106

De Santis S, Jones DK, Roebroeck A (2016) Including diffusion time dependence in the extra-axonal space improves in vivo estimates of axonal diameter and density in human. white matter. Neuroimage 130:91–103. https://doi.org/10.1016/j.neuroimage.2016.01.047

Dell'Acqua F, Rizzo G, Scifo P, Clarke RA, Scotti G, Fazio F (2007) A model-based deconvolution approach to solve fiber crossing in diffusion-weighted MR imaging. IEEE Trans Biomed Eng 54:462–472. https://doi.org/10.1109/TBME.2006.888830

Dhital B, Reisert M, Kellner E, Kiselev VG (2019) Intra-axonal diffusivity in brain white matter. NeuroImage 189:543–550

Dorkenwald S, Schubert PJ, Killinger MF, Urban G, Mikula S, Svara F, Kornfeld J (2017) Automated synaptic connectivity inference for volume electron microscopy. Nat Methods 14:435–442. https://doi.org/10.1038/nmeth.4206

Duval T et al (2015) In vivo mapping of human spinal cord microstructure at 300 mT/m. Neuroimage 118:494–507. https://doi.org/10.1016/j.neuroimage.2015.06.038

Fieremans E, Burcaw LM, Lee HH, Lemberskiy G, Veraart J, Novikov DS (2016) In vivo observation and biophysical interpretation of time-dependent diffusion in human white matter. Neuroimage 129:414–427. https://doi.org/10.1016/j.neuroimage.2016.01.018

Frank LR (2002) Characterization of anisotropy in high angular resolution diffusion-weighted MRI. Magn Reson Med 47(6):1083–1099

Giacci MK, Bartlett CA, Huynh M, Kilburn MR, Dunlop SA, Fitzgerald M (2018) Three dimensional electron microscopy reveals changing axonal and myelin morphology along normal and partially injured optic nerves. Sci Rep 8:3979. https://doi.org/10.1038/s41598-018-22361-2

Grussu F, Schneider T, Yates RL, Zhang H, Wheeler-Kingshott C, DeLuca GC, Alexander DC (2016) A framework for optimal whole-sample histological quantification of neurite orientation dispersion in the human spinal cord. J Neurosci Methods 273:20–32. https://doi.org/10.1016/j.jneumeth.2016.08.002

Jespersen SN, Kroenke CD, Ostergaard L, Ackerman JJ, Yablonskiy DA (2007) Modeling dendrite density from magnetic resonance diffusion measurements. Neuroimage 34:1473–1486. https://doi.org/10.1016/j.neuroimage.2006.10.037

Jespersen SN et al (2010) Neurite density from magnetic resonance diffusion measurements at ultrahigh field: comparison with light

microscopy and electron microscopy. Neuroimage 49:205–216. https://doi.org/10.1016/j.neuroimage.2009.08.053
Jespersen SN, Olesen JL, Hansen B, Shemesh N (2017) Diffusion time dependence of microstructural parameters in fixed spinal cord. Neuroimage. https://doi.org/10.1016/j.neuroimage.2017.08.039
Jones DK (2010) Diffusion MRI: theory, methods, and application. Oxford University Press, Oxford
Kaynig V et al (2015) Large-scale automatic reconstruction of neuronal processes from electron microscopy images. Med Image Anal 22:77–88. https://doi.org/10.1016/j.media.2015.02.001
Kirschner DA, Hollingshead CJ (1980) Processing for electron microscopy alters membrane structure and packing in myelin. J Ultrastruct Res 73:211–232
Kleinnijenhuis M, Johnson E, Mollink J, Jbabdi S, Miller K (2017) A 3D electron microscopy segmentation pipeline for hyper-realistic diffusion simulations. In: ISMRM 25th annual meeting, Hawaii, USA Proceedings of the ISMRM annual meeting, vol 25, p 1090
Komlosh ME, Ozarslan E, Lizak MJ, Horkayne-Szakaly I, Freidlin RZ, Horkay F, Basser PJ (2013) Mapping average axon diameters in porcine spinal cord white matter and rat corpus callosum using d-PFG. MRI Neuroimage 78:210–216. https://doi.org/10.1016/j.neuroimage.2013.03.074
Lee H-H, Fieremans E, Novikov DS (2017) What dominates the time dependence of diffusion transverse to axons: intra- or extra-axonal water? NeuroImage. https://doi.org/10.1016/j.neuroimage.2017.12.038
Leergaard TB, White NS, de Crespigny A, Bolstad I, D'Arceuil H, Bjaalie JG, Dale AM (2010) Quantitative histological validation of diffusion MRI fiber orientation distributions in the rat brain. PLoS One 5:e8595. https://doi.org/10.1371/journal.pone.0008595
Liewald D, Miller R, Logothetis N, Wagner HJ, Schuz A (2014) Distribution of axon diameters in cortical white matter: an electron-microscopic study on three human brains and a macaque. Biol Cybern 108:541–557. https://doi.org/10.1007/s00422-014-0626-2
Little GJ, Heath JW (1994) Morphometric analysis of axons myelinated during adult life in the mouse superior cervical ganglion. J Anat 184(Pt 2):387–398
Maco B, Cantoni M, Holtmaat A, Kreshuk A, Hamprecht FA, Knott GW (2014) Semiautomated correlative 3D electron microscopy of in vivo-imaged axons and dendrites. Nat Protoc 9:1354–1366. https://doi.org/10.1038/nprot.2014.101
Marzan DE, West BL, Salzer JL (2018) Microglia are necessary for toxin-mediated demyelination and activation of microglia is sufficient to induce demyelination. https://doi.org/10.1101/501148
Mason JL, Langaman C, Morell P, Suzuki K, Matsushima GK (2001) Episodic demyelination and subsequent remyelination within the murine central nervous system: changes in axonal calibre. Neuropathol Appl Neurobiol 27:50–58
Mollink J et al (2017) Evaluating fibre orientation dispersion in white matter: comparison of diffusion MRI, histology and polarized light imaging. Neuroimage 157:561–574. https://doi.org/10.1016/j.neuroimage.2017.06.001
Neuman C (1974) Spin echo of spins diffusing in a bounded medium. J Chem Phys 60:4508–4511
Novikov DS, Jensen JH, Helpern JA, Fieremans E (2014) Revealing mesoscopic structural universality with diffusion. Proc Natl Acad Sci USA 111:5088–5093. https://doi.org/10.1073/pnas.1316944111
Novikov DS, Fieremans E, Jespersen SN, Kiselev VG (2018a) Quantifying brain microstructure with diffusion MRI: theory and parameter estimation. NMR Biomed. https://doi.org/10.1002/nbm.3998
Novikov DS, Kiselev VG, Jespersen SN (2018b) On modeling. Magn Reson Med 79:3172–3193. https://doi.org/10.1002/mrm.27101
Novikov DS, Veraart J, Jelescu IO, Fieremans E (2018c) Rotationally-invariant mapping of scalar and orientational metrics of neuronal microstructure with diffusion MRI. Neuroimage. https://doi.org/10.1016/j.neuroimage.2018.03.006
Perge JA, Koch K, Miller R, Sterling P, Balasubramanian V (2009) How the optic nerve allocates space, energy capacity, and information. J Neurosci 29(24):7917–7928
Politis A (2016) Microphone array processing for parametric spatial audio techniques. http://urn.fi/URN:ISBN:978-952-60-7037-7
Reisert M, Kellner E, Dhital B, Hennig J, Kiselev VG (2017) Disentangling micro from mesostructure by diffusion MRI: a Bayesian approach. Neuroimage 147:964–975. https://doi.org/10.1016/j.neuroimage.2016.09.058
Ronen I, Budde M, Ercan E, Annese J, Techawiboonwong A, Webb A (2014) Microstructural organization of axons in the human corpus callosum quantified by diffusion-weighted magnetic resonance spectroscopy of *N*-acetylaspartate and post-mortem histology. Brain Struct Funct 219:1773–1785. https://doi.org/10.1007/s00429-013-0600-0
Salo RA, Belevich I, Manninen E, Jokitalo E, Grohn O, Sierra A (2018) Quantification of anisotropy and orientation in 3D electron microscopy and diffusion tensor imaging in injured rat brain. Neuroimage 172:404–414. https://doi.org/10.1016/j.neuroimage.2018.01.087
Schilling K, Janve V, Gao Y, Stepniewska I, Landman BA, Anderson AW (2016) Comparison of 3D orientation distribution functions measured with confocal microscopy and diffusion. MRI Neuroimage 129:185–197. https://doi.org/10.1016/j.neuroimage.2016.01.022
Schilling KG, Janve V, Gao Y, Stepniewska I, Landman BA, Anderson AW (2018) Histological validation of diffusion MRI fiber orientation distributions. and dispersion. Neuroimage 165:200–221. https://doi.org/10.1016/j.neuroimage.2017.10.046
Schneider R, Weil W (2008) Stochastic and integral geometry. Springer, Berlin
Sepehrband F, Alexander DC, Clark KA, Kurniawan ND, Yang Z, Reutens DC (2016a) Parametric probability distribution functions for axon diameters of corpus callosum. Front Neuroanat 10:59. https://doi.org/10.3389/fnana.2016.00059
Sepehrband F, Alexander DC, Kurniawan ND, Reutens DC, Yang Z (2016b) Towards higher sensitivity and stability of axon diameter estimation with diffusion-weighted MRI. NMR Biomed 29:293–308. https://doi.org/10.1002/nbm.3462
Shepherd GM, Raastad M, Andersen P (2002) General and variable features of varicosity spacing along unmyelinated axons in the hippocampus and cerebellum. Proc Natl Acad Sci USA 99:6340–6345. https://doi.org/10.1073/pnas.052151299
Sommer C, Straehle C, Koethe U, Hamprecht FA (2011) Ilastik: interactive learning and segmentation toolkit. In: Biomedical imaging: from nano to macro, 2011 IEEE international symposium on IEEE, pp 230–233
Sotiropoulos SN, Behrens TE, Jbabdi S (2012) Ball and rackets: inferring fiber fanning from diffusion-weighted. MRI Neuroimage 60:1412–1425. https://doi.org/10.1016/j.neuroimage.2012.01.056
Stikov N, Perry LM, Mezer A, Rykhlevskaia E, Wandell BA, Pauly JM, Dougherty RF (2011) Bound pool fractions complement diffusion measures to describe white matter micro and macrostructure. Neuroimage 54:1112–1121. https://doi.org/10.1016/j.neuroimage.2010.08.068
Stikov N et al (2015) In vivo histology of the myelin g-ratio with magnetic resonance imaging. Neuroimage 118:397–405. https://doi.org/10.1016/j.neuroimage.2015.05.023
Straehle CN, Kothe U, Knott G, Hamprecht FA (2011) Carving: scalable interactive segmentation of neural volume electron microscopy images. Med Image Comput Comput Assist Interv 14:653–660
Sturrock RR (1980) Myelination of the mouse corpus callosum. Neuropathol Appl Neurobiol 6:415–420

Sun D, Roth S, Black MJ (2010) Secrets of optical flow estimation and their principles. In: Computer vision and pattern recognition (CVPR), 2010 IEEE conference on IEEE, pp 2432–2439

Sun D, Roth S, Black MJ (2014) A quantitative analysis of current practices in optical flow estimation and the principles behind them. Int J Comput Vis 106:115–137

Tang-Schomer MD, Johnson VE, Baas PW, Stewart W, Smith DH (2012) Partial interruption of axonal transport due to microtubule breakage accounts for the formation of periodic varicosities after traumatic axonal injury. Exp Neurol 233:364–372. https://doi.org/10.1016/j.expneurol.2011.10.030

Tariq M, Schneider T, Alexander DC, Gandini Wheeler-Kingshott CA, Zhang H (2016) Bingham-NODDI: mapping anisotropic orientation dispersion of neurites using diffusion. MRI Neuroimage 133:207–223. https://doi.org/10.1016/j.neuroimage.2016.01.046

Tournier JD, Calamante F, Connelly A (2007) Robust determination of the fibre orientation distribution in diffusion MRI: non-negativity constrained super-resolved spherical deconvolution. Neuroimage 35:1459–1472. https://doi.org/10.1016/j.neuroimage.2007.02.016

Veraart J, Fieremans E, Novikov DS (2018a) On the scaling behavior of water diffusion in human brain white matter. Neuroimage. https://doi.org/10.1016/j.neuroimage.2018.09.075

Veraart J, Novikov DS, Fieremans E (2018b) TE dependent diffusion imaging (TEdDI) distinguishes between compartmental T-2 relaxation times. Neuroimage 182:360–369. https://doi.org/10.1016/j.neuroimage.2017.09.030

West KL, Kelm ND, Carson RP, Does MD (2015) Quantitative analysis of mouse corpus callosum from electron microscopy images. Data Brief 5:124–128. https://doi.org/10.1016/j.dib.2015.08.022

West KL, Kelm ND, Carson RP, Does MD (2016) A revised model for estimating g-ratio from MRI. Neuroimage 125:1155–1158. https://doi.org/10.1016/j.neuroimage.2015.08.017

Wilke SA et al (2013) Deconstructing complexity: serial block-face electron microscopic analysis of the hippocampal mossy fiber synapse. J Neurosci 33:507–522. https://doi.org/10.1523/JNEUROSCI.1600-12.2013

Womersley RS (2017) Efficient spherical designs with good geometric properties. Contemporary computational mathematics - A celebration of the 80th birthday of Ian Sloan. Springer, Cham, pp 1243–1285

Yang HJ, Vainshtein A, Maik-Rachline G, Peles E (2016) G protein-coupled receptor 37 is a negative regulator of oligodendrocyte differentiation and myelination. Nat Commun 7:10884. https://doi.org/10.1038/ncomms10884

Zaimi A, Wabartha M, Herman V, Antonsanti PL, Perone CS, Cohen-Adad J (2018) AxonDeepSeg: automatic axon and myelin segmentation from microscopy data using convolutional neural networks. Sci Rep 8:3816. https://doi.org/10.1038/s41598-018-22181-4

Zhang H, Schneider T, Wheeler-Kingshott CA, Alexander DC (2012) NODDI: practical in vivo neurite orientation dispersion and density imaging of the human brain. Neuroimage 61:1000–1016. https://doi.org/10.1016/j.neuroimage.2012.03.072